SAE INTERNATIONAL

ARTICLE INFO
Article ID: 14-14-01-0003

doi:10.4271/14-14-01-0003

Model-Based State-of-Charge Estimation of 28 V $LiFePO_4$ Aircraft Battery

Yizhao Gao,[1] Trung Nguyen,[2] and Simona Onori[1]

[1]*Stanford University, Department of Energy Science and Engineering, USA*
[2]*EIC Laboratories, Inc., USA*

Abstract

This article introduces an advanced state-of-charge (SOC) estimation method customized for 28 V $LiFePO_4$ (LFP) helicopter batteries. The battery usage profile is characterized by four consecutive current pulses, each corresponding to distinct operational phases on the helicopter: instrument check, key-on, recharge, and emergency power output stages. To establish a precise battery model for LFP cells, the parameters of a second-order equivalent-circuit model are identified as a function of C-rate, SOC, and temperature. Furthermore, the observability of the battery model is assessed using extended Lie derivatives. The signal-to-noise ratio (SNR) of the open-circuit voltage (OCV)–SOC relation is analyzed and employed to evaluate the estimator's resilience against OCV flatness. The extended Kalman filter (EKF) and the unscented Kalman filter (UKF) are utilized for SOC estimation. The results emphasize the significance of meticulously choosing process and sensor noise covariance matrices to achieve a resilient SOC estimator for LFP cells. Furthermore, the UKF demonstrates superior robustness against OCV–SOC relationships compared to the EKF. Lastly, the UKF is selected for testing across various aircraft usage scenarios at 10°C, 25°C, and 45°C. The resultant root mean square errors for SOC estimation at these different temperatures are consistently below 2%, thereby validating the effectiveness of the UKF SOC estimation approach.

History

Received: 17 Jan 2024
Revised: 03 Jun 2024
Accepted: 15 Jul 2024
e-Available: 01 Aug 2024

Keywords

LFP batteries, Parameter identification, State estimation, Signal-to-noise ratio, Observability analysis, EKF, UKF

Citation

Gao, Y., Nguyen, T., and Onori, S., "Model-Based State-of-Charge Estimation of 28 V $LiFePO_4$ Aircraft Battery," *SAE Int. J. Elect. Veh.* 14(1):2025, doi:10.4271/14-14-01-0003.

ISSN: 2691-3747
e-ISSN: 2691-3755

1. Introduction

As auxiliary power sources for aircraft, aviation battery packs primarily serve as emergency and engine-starting power sources [1]. Their main applications are as follows [2]: (1) acting as a vital emergency power source, ensuring a stable power supply to critical onboard systems during fluctuations in generator power; (2) supplying electrical power for checking instruments and starting the engine of the aircraft; (3) mitigating transient voltage fluctuations during onboard power source transitions. In the aviation sector, lithium-ion battery packs have gained prominence [3], and $LiFePO_4$ (LFP) battery technology has emerged as the preferred choice due to its thermal stability and cost-effectiveness [4].

Monitoring lithium-ion batteries in real time necessitates a battery management system (BMS) [5]. State-of-charge (SOC) estimation is one of the fundamental functions of BMS [6, 7]. Coulomb counting is a straightforward method to estimate the cell SOC, involving current integration over time [8]. However, as an open-loop estimation method, Coulomb counting is sensitive to initial SOC and current sampling accuracy [9]. To enhance SOC estimation robustness, Kalman filter (KF)-based estimation algorithms including the unscented Kalman filter (UKF) and extended Kalman filter (EKF) are employed to enable closed-loop estimation [10]. In EKF- and UKF-based SOC estimation methods, the difference between the battery model predicted output and measurements at the present step is fed back to the observer to correct the estimated states [11, 12]. EKF relies on linearized battery governing equations, may introduce errors, especially for highly nonlinear models [13, 14], whereas UKF utilizes the unscented transform to derive statistics for the process noise covariance [15], eliminating the need to compute derivatives of the battery model [16]. UKF has been shown to outperform the EKF regarding estimation accuracy while maintaining compatible computational complexity [17].

OCV–SOC lookup table is employed in EKF and UKF for SOC estimations [18]. For LFP batteries, OCV–SOC curves are relatively flat, increasing the SOC estimation uncertainty. In [19], OCV is divided into three regions: plateau range, steep-slope range, and gentle-slope range. Only the gentle-slope range is used in the closed-loop SOC estimation. In [20], two consecutive linear filtering stages are used for OCV estimation. In the initial stage, a recursive least squares filter is employed to evaluate the parameters of the equivalent-circuit model (ECM), and a fading Kalman filter compensating for LFP OCV modeling errors with a forgetting factor is used in the second stage. In [21], a weighted average function integrates SOC estimation obtained through Coulomb counting and the OCV-based method to forecast the SOC in the LFP battery pack. In [22], a pseudo-OCV is introduced to create a comprehensive LFP OCV for SOC estimation. The SOC estimation error across the entire range remains below 3%. Although the reconstructed LFP OCV improves OCV slopes, it does introduce voltage errors. In [23], differential voltage (DV) analysis is used as an indicator for inferring SOC information. To ensure robust SOC and capacity estimation, three feature points (at 13%, 70%, and 92.5% SOC positions) are captured from the incremental capacity (IC) or DV curves [24]. It is important to note that IC curve- and DV curve-based SOC estimation schemes are most effective when applied under conditions of low C-rate currents. Utilizing the single particle model (SPM), the concentration of lithium ions within the phase-changing electrodes was estimated considering the phase-moving boundary in an LFP electrode [25]. In [26], the electrochemical impedance spectroscopy (EIS) of $LFPLi_4Ti_5O_{12}$ cells was studied, which showed a strong dependence on SOC at reasonably fast frequencies ($\omega >$ 1 rad/s). Such impedance was then used as a distinctive feature for accurately identifying the SOC [26]. Additionally, the expansion force of LFP pouch cells is employed as an essential parameter for SOC estimation [27, 28]. The force-aided SOC estimation method offers improved accuracy compared to voltage-based methods, although real-time measurement of battery force remains challenging.

Evaluating battery model observability is a crucial step before designing state estimation algorithms [29]. For a nonlinear ECM, the observability matrix is derived using the Lie derivative [30]. A nonlinear battery model is deemed weakly observable when its observability matrix is full rank, enabling the exclusive reconstruction of states through output measurements and input [31]. The condition number of the observability matrix gauges the degree of measurement errors that impact estimation results. A high condition number implies that even a small measurement noise could be magnified, resulting in substantial errors in state estimation [32, 33]. In [34], the influence of current, uncertain parameters, and fitting methods of OCV on ECM observability were investigated.

The signal-to-noise ratio (SNR) of OCV is defined as:

$$SNR_{OCV}\left(OCV,noise\right) = 20\log_{10}\left(\frac{\sqrt{\Sigma_{n=1}^{N}\left|OCV_n\right|^2}}{\sqrt{\Sigma_{n=1}^{N}\left|noise_n\right|^2}}\right) \quad \text{Eq. (1)}$$

$$n = 1,\ldots,N$$

where *OCV* and *noise* values are stored as vectors of length *N*. OCV_n and $noise_n$ are the *n*th value in the *OCV* and noise vectors, respectively. Generally, a high *SNR* means less noise is mixed with the signal and better signal quality is achieved. Hence, a high *SNR* value is desirable for state estimation. The noise can arise from errors in voltage measurement and inaccuracies in the model's output voltage predictions. More specifically, voltage measurement errors may stem from inaccuracies in the voltage sensors, while inaccuracies in the battery model can result in errors in output voltage predictions [35].

For LFP cells, the flat OCV–SOC profiles can lead to a low SNR [36, 37]. The impact of low SNR in the flat OCV region on estimator performance has not been fully explored. Extended Lie derivatives, an enhanced version of Lie derivatives, consider the effects of input and its derivatives on system observability [38]. Given the substantial impact of input current on system observability, investigating system observability using extended Lie derivatives is critical.

SOC estimation algorithms necessitate validation data from operational profiles under representative conditions [39]. While automotive battery testing often uses driving profiles like the Federal Urban Driving Schedule (FUDS) [40], or its European [41] or Asian equivalents [42], aviation-specific battery usage profiles that encompass representative operating conditions are scarce [43].

Several research gaps in SOC estimation for LFP batteries employed as auxiliary power sources in aviation applications can be outlined as follows. Most SOC estimation algorithms have been developed and validated in the context of electric vehicle scenarios. In contrast, research on SOC estimation for aviation applications is limited. For ECM-based SOC estimators, understanding the model observability with extended Lie derivative and its impact on estimator's performance are still lacking. In the case of LFP cells, the effects of OCV flatness on SOC estimation by observers need to be quantified and investigated. The LFP cell hysteresis is not modeled in this article since the operating conditions targeted in this work are primarily for the discharge conditions of the battery.

The following contributions have been made to this article:

1. Due to the lack of accessible datasets on helicopter battery duty cycles, we characterized the aviation duty cycle and collected data at three temperatures across five LFP cells.
2. We identified and validated a second-order ECM based on SOC, temperature, and current, investigating its observability using extended Lie derivatives.
3. We introduced the SNR to quantify the impact of LFP OCV flatness on SOC estimator performance.
4. We designed and validated EKF and UKF algorithms for SOC estimation, calibrating the filters based on a sensitivity study of process covariance (Q) and measurement noise covariance (R).

2. Duty Cycle Development and Experimental Tests

The 28 V lithium-ion battery pack shown in Figure 1 (in orange) is used as an auxiliary power and emergency energy source [44]. As shown in Figure 2, the battery pack

FIGURE 1 28 V Li-ion aircraft battery.

Reprinted with permission from Ref. [44]. © EIC Labs

considered in this study consists of eight modules connected in series, where each module is composed of four cells connected in parallel. Hence, the overall configuration of the battery pack is 4P8S.

As depicted in Figure 2, the pack voltage V_{pack} and pack current i_{pack} are derived from the cell voltages V_{cell} and cell current i_{cell} as follows:

$$V_{pack} = N_s * V_{cell} \quad N_s = 8 \qquad \text{Eq. (2)}$$

$$i_{pack} = N_p * i_{cell} \quad N_p = 4 \qquad \text{Eq. (3)}$$

and the power output of the battery pack P_{pack} is described as:

$$P_{pack} = V_{pack} * i_{pack} = N_s * N_p * V_{cell} * i_{cell} \qquad \text{Eq. (4)}$$

In this study, the heterogeneity within the cells is ignored [45].

The battery pack operates through five consecutive phases: rest, instrument check, key-on, recharge, and

FIGURE 2 28 V LFP battery pack topology (4P8S).

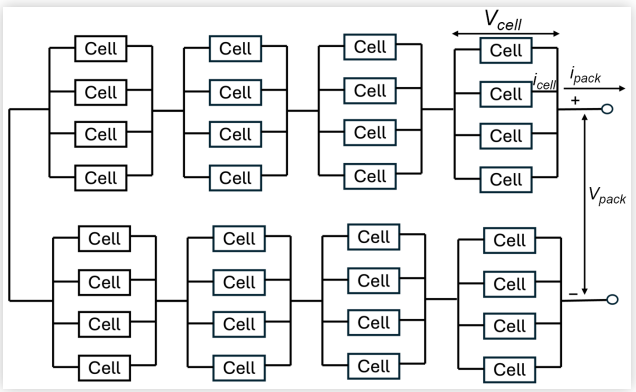

© SAE International

FIGURE 3 Duty cycle of the aircraft batteries composed of four constituent stages: instrument check (duration—t_1, current—I_1), key-on (duration—t_2, current—I_2), recharge (duration—t_3, current—I_3), and emergency power output (duration—t_4, current—I_4), respectively. The signs of the discharge current and charge current are positive and negative, respectively.

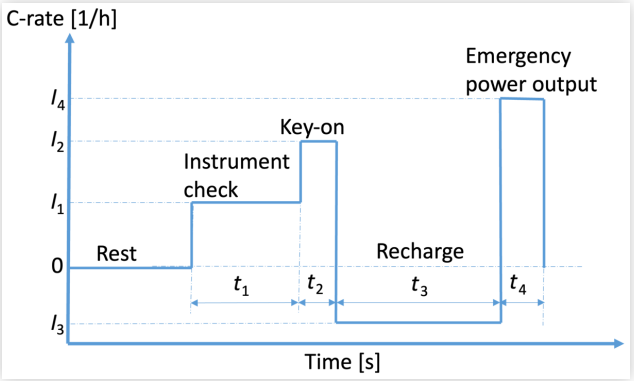

emergency power output, as illustrated in Figure 3. The duty cycle is designed to simulate the operating conditions of an aviation battery pack. C-rate is a measure of the rate at which a battery is discharged relative to its nominal capacity. The signs of the discharge current and charge current are positive and negative, respectively. The detailed modeling of helicopter dynamics including motor and drivetrain characteristics is not within the scope of this article. The design principles of these phases are detailed as follows.

- **Instrument check (Duration: t_1):** The battery is discharged at a low C-rate for the pilot to check the instruments before starting the engine. The applied current in this stage is denoted as I_1.
- **Key-on (Duration: t_2):** The battery is discharged at a moderate C-rate for a short period to ignite the engine. The applied current in this stage is denoted as I_2.
- **Recharge (Duration: t_3):** The battery is charged at a low C-rate for a long duration. The applied current in this stage is denoted as I_3.
- **Emergency power output (Duration: t_4):** The battery is discharged at a high C-rate to meet the power requirements such as emergent take-off and landing. The applied current in this stage is denoted as I_4.

In this study, three different usage profiles are designed by adjusting the length of t_1, t_2, t_3, and t_4, as shown in Table 1. In Scenario 1 (S1), the duty cycle is designed to simulate a long-time emergency power output requirement, with t_4 set to 600 s. Conversely, in Scenario 2 (S2), the duty cycle simulates a short-time emergency power output, with the emergency power output duration t_4 set to 200 s. Finally, in Scenario 3 (S3), the duty cycle simulates a long-time instrument check, with the duration of the instrument check t_1 set to 600 s. Three aircraft usage profiles (S1, S2, and S3) are employed to 26,650 cylindrical LFP cells whose specifications are listed in Table 2.

TABLE 1 Duty cycle scenarios.

	t_1 [s]	t_2 [s]	t_3 [s]	t_4 [s]
Scenario 1 (S1): long-time emergency output	150	20	200	600
Scenario 2 (S2): short-time emergency output	150	20	200	200
Scenario 3 (S3): long-time instrument check	600	20	200	100

Here, I_1, I_2, I_3, and I_4 are set to 0.3C (0.75A), 0.7C (1.75A), −0.1C (0.25A), and 1C (2.5A), respectively, to generate representative battery usage profile for the 28 V aviation batteries used in this article.

The cell testing equipment available at the Stanford Energy Control Lab is depicted in Figure 4 [46]. The cells are placed in the AMEREX IC500R thermal chamber and are cycled using the Arbin LBT21024.

The LFP cells are tested at three temperatures (10°C, 25°C, and 45°C). The 1C cell capacity test, galvanostatic intermittent titration technique (GITT) test, UDDS test, and experiments with three aircraft usage profiles are conducted.

For 1C cell capacity test, the cell is first charged fully with a constant current–constant voltage (CC-CV) protocol at 1C until the cell voltage reaches the upper cut-off voltage of 3.65 V. Then the cell voltage is maintained at 3.65 V until the cell current decreases to 1/30C. After 1-h rest, the cell is discharged at 1C until the cell voltage reaches 2.0 V. The capacity test results for five cells are listed in Appendix A. For GITT discharge testing shown in Figure 5, the cell is first fully charged, and then the GITT is conducted, employing a constant current titration (0.2C) of 10% SOC increment. A 2-h rest period ensures the cells reach equilibrium, and the voltage at the end of each rest period is extracted and plotted against SOC to generate the discharging OCV. The GITT protocol is performed throughout the entire SOC range until the cell terminal voltage drops to a lower cut-off voltage of 2.1 V. For the charging GITT, the magnitude and duration of the charging current during the charging GITT procedure are the same as those of the discharging GITT procedure. The charging GITT test stops when the cell voltage reaches the upper cut-off voltage of 3.65 V. The UDDS tests are conducted for ECM validation.

TABLE 2 26,650 cylindrical LFP cell specification.

Nominal capacity	2.5 Ah
Nominal voltage	3.3 V
Cathode chemistry	$LiFePO_4$
Anode chemistry	Graphite

FIGURE 4 Battery testing equipment at Stanford Energy Control Lab.

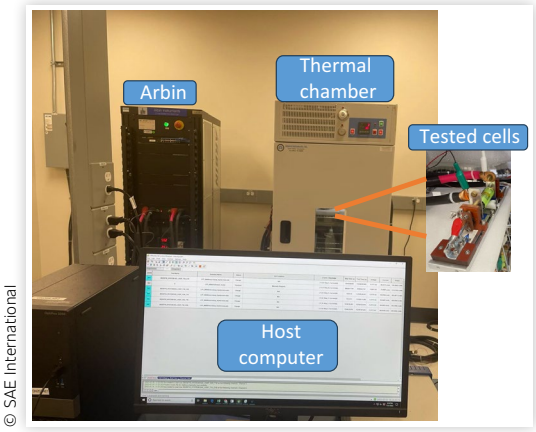

3. ECM Parameter Identification

In this section, a second-order ECM is formulated. The governing equations of the ECM are:

$$V(t) = OCV(SOC,T) - V_1 - V_2 - R_0 * i(t) \quad \text{Eq. (5)}$$

$$\dot{V}_1 = \frac{1}{C_1} i(t) - \frac{1}{R_1 C_1} V_1 \quad \text{Eq. (6)}$$

$$\dot{V}_2 = \frac{1}{C_2} i(t) - \frac{1}{R_2 C_2} V_2 \quad \text{Eq. (7)}$$

$$\dot{SOC} = \frac{-1}{3600 * Q_{cell}} i(t) \quad \text{Eq. (8)}$$

where $V(t)$ is the battery terminal voltage; two RC branches (R_1, C_1, R_2, C_2) are used to model the dynamic response of the cell voltage; V_1 and V_2 are the voltage across R_1 and R_2, respectively; $i(t)$ is the input current; and R_0 is the series resistance. The RC parameters (R_1, C_1, R_2, C_2) depend on SOC, temperature T, and directional current i; OCV is a nonlinear function of SOC and temperature T; $\dot{V}_1$, $\dot{V}_2$, and $\dot{SOC}$ are the time derivatives of V_1, V_2, and SOC, respectively.

The state-space representation of the second-order ECM is given by:

$$\underbrace{\begin{bmatrix} \dot{V}_1 \\ \dot{V}_2 \\ \dot{SOC} \end{bmatrix}}_{\dot{x}} = \underbrace{\begin{bmatrix} \frac{-1}{R_1 C_1} & 0 & 0 \\ 0 & \frac{-1}{R_2 C_2} & 0 \\ 0 & 0 & 0 \end{bmatrix}}_{A} \underbrace{\begin{bmatrix} V_1 \\ V_2 \\ SOC \end{bmatrix}}_{x} + \underbrace{\begin{bmatrix} \frac{1}{C_1} \\ \frac{1}{C_2} \\ \frac{-1}{3600 \cdot Q_{cell}} \end{bmatrix}}_{B} i \quad \text{Eq. (9)}$$

where $x = [V_1, V_2, SOC]$ is the state vector A and B are the state and input matrices, respectively.

3.1. RC Parameter Identification Results

In this section, the RC parameters of the battery models are determined using the GITT data. The OCV is determined by cycling the battery with the discharging GITT

FIGURE 5 GITT test procedure (T = 25°C) at discharge and charge directions. (a) Charge GITT current profile. (b) Discharge GITT current profile. (c) Charge GITT voltage and SOC. (d) Discharge GITT voltage and SOC.

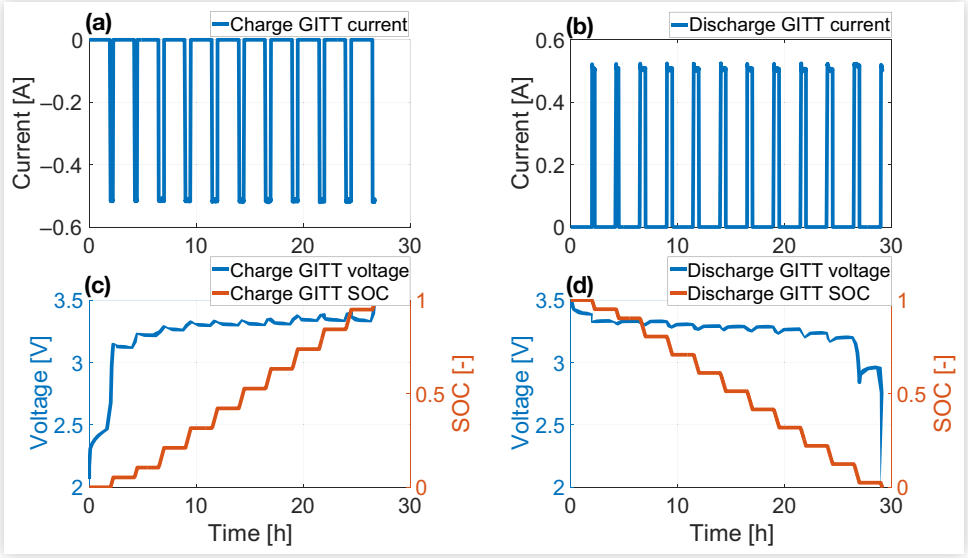

FIGURE 6 Discharge OCV versus SOC at 10°C, 25°C, and 45°C.

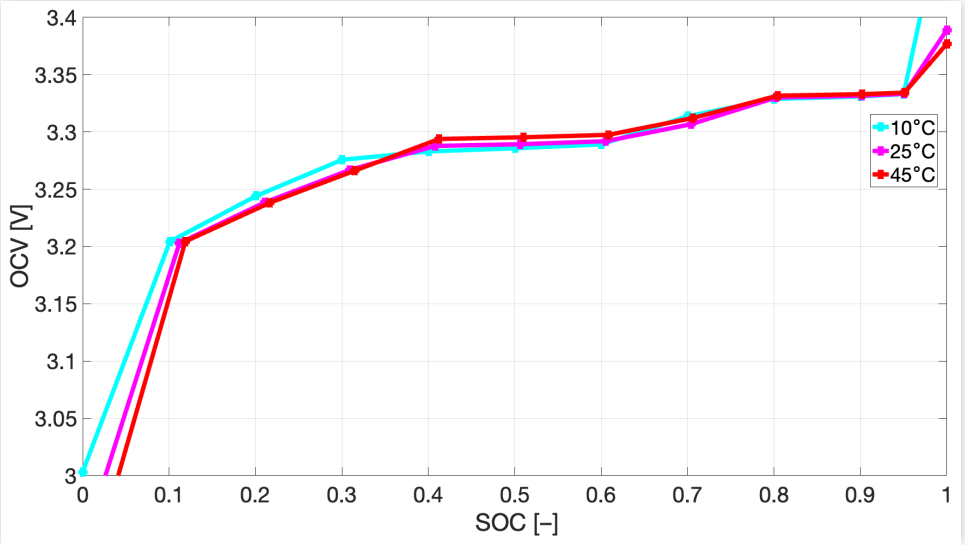

data as shown in Figure 5. The cell OCV versus SOC profiles at 10°C, 25°C, and 45°C are plotted in Figure 6. It can be found that the OCV demonstrates dependency on temperature and current direction. R_0 is identified using the voltage drop over the pulse current. Time constants are determined by fitting the ECM voltage to the experimental voltage relaxation process. Finally, R_1 and R_2 are identified by fitting the ECM voltage to the experimental voltage with pulse and relaxation process. The RC parameter identification process and identification results are elaborated in Appendix B. The identified R_0 at 10°C, 25°C, and 45°C are plotted in Figure 7. The identified ECM is validated with the experimental UDDS data as shown in Figure 8. The RMSEs of the voltage predictions are 5.3 mV, 5.0 mV, 4.7 mV at 10°C, 25°C, and 45°C, respectively. These results validate the identified ECM.

3.2. ECM Observability Analysis with Extended Lie Derivative

The observability of the battery model is investigated using the extended Lie derivatives [47]. For a nonlinear system given by:

$$\dot{x} = f\left(x,u\right) \quad \text{Eq. (10)}$$

$$y = h\left(x,u\right) \quad \text{Eq. (11)}$$

where $x\epsilon R^n$ denotes the state vector, $u\epsilon R^p$ is the system input vector, and $y\epsilon R^m$ is the system output; $f(x, u)$ is the state-space representation of the ECM as shown in Equations 2 and 3; $h(x, u)$ is a smooth continuous nonlinear function as shown in Equation 1. The observability matrix $\mathcal{O}$ is calculated with extended Lie derivatives L_f^{n-1} [29]:

FIGURE 7 Cell R_0 identification results as a function of SOC, current, and temperature.

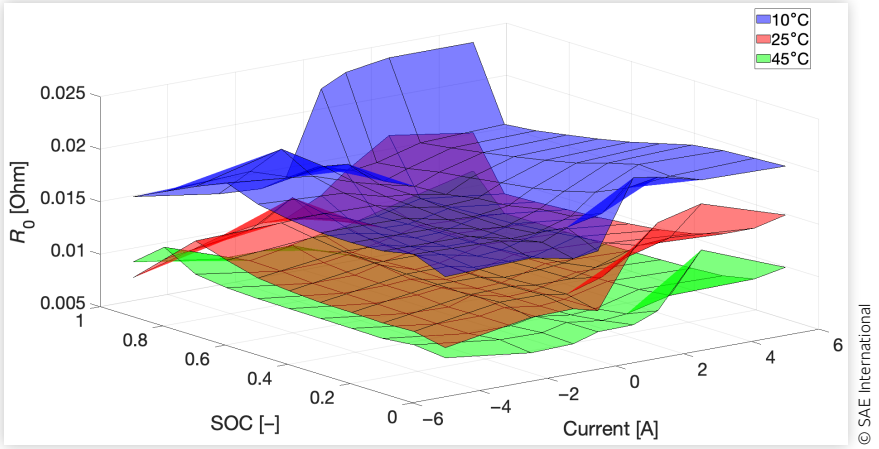

FIGURE 8 ECM predicted voltage vs. experimental voltage with UDDS profiles (a) at 10°C (b), 25°C (d), and 45°C (f); Voltage prediction error at 10°C (c), 25°C (e), and 45°C (g).

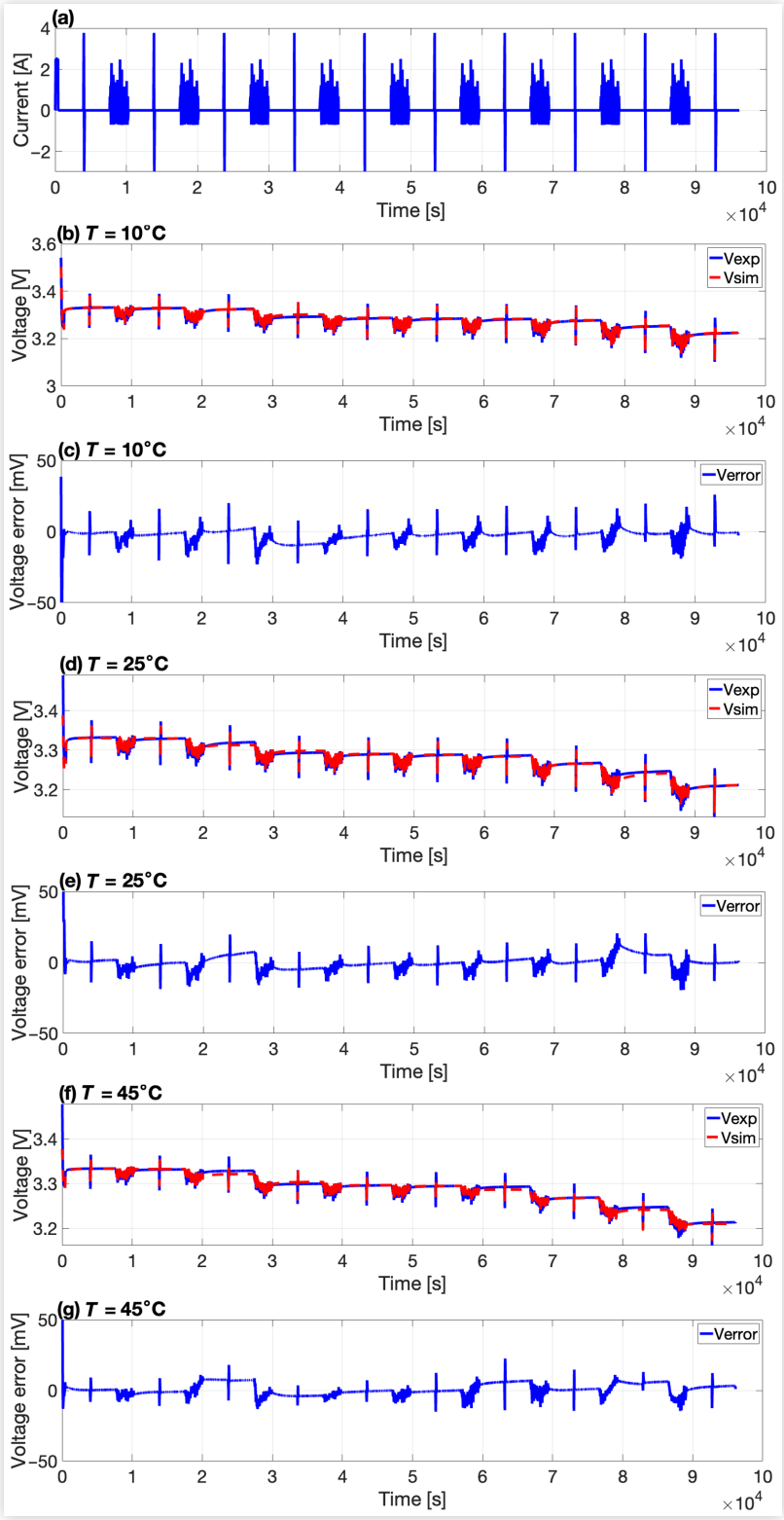

$$\mathcal{O} = \frac{d}{dx}\begin{bmatrix} L_f^0(h) \\ L_f^1(h) \\ \vdots \\ L_f^{n-1}(h) \end{bmatrix} \quad \text{Eq. (12)}$$

where

$$L_f^0(h) = y = h(x,u)$$
$$L_f^1(h) = \dot{y} = \dot{h}(x,u,\dot{u}) = h_x(x,u)f(x,u) + h_u(x,u)\dot{u}$$
$$L_f^2(h) = \ddot{y} = \ddot{h}(x,u,\dot{u},\ddot{u})$$
$$= \dot{h}_x(x,u,\dot{u})f(x,u) + \dot{h}_u(x,u,\dot{u})\dot{u} + h_{\dot{u}}(x,u,\dot{u})\ddot{u}$$
$$\vdots$$
$$L_f^n(h) = y^n = \frac{\partial y^{n-1}}{\partial x}\frac{dx}{dt} + \sum_{i=0}^{n-1}\frac{\partial y^{n-1}}{\partial u^i}\frac{du^i}{dt}$$

where $\dot{y}$ and $\ddot{y}$ are the first and second derivative of y with respect to time t, respectively; h_x and h_u are the derivatives of h with respect to x and u, respectively.

For a second ECM expressed in Equation 9, the state-space presentation f can be written as:

$$f_{3\times1} = \begin{bmatrix} \underbrace{\frac{V_1}{R_1C_1} + \frac{1}{C_1}i}_{f_1} \\ \underbrace{\frac{V_2}{R_2C_2} + \frac{1}{C_2}i}_{f_2} \\ \underbrace{\frac{-1}{3600\cdot Q_{cell}}i}_{f_3} \end{bmatrix} \quad \text{Eq. (13)}$$

Furthermore, the extended Lie derivatives of the voltage (Equation 5) with respect to x are calculated as:

$$L_f^0(h) = OCV - V_1 - V_2 - iR_0;$$
$$L_f^1(h) = \frac{dL_f^0(h)}{dV_1} * f_1 + \frac{dL_f^0(h)}{dV_2} * f_2 + \frac{dL_f^0(h)}{dV_3} * f_3 + \frac{dL_f^0(h)}{di} * \frac{di}{dt} = -\frac{i}{c_1} - \frac{i}{c_2} + \frac{V_1}{R_1c_1} + \frac{V_2}{R_2c_2} - R_0\frac{di}{dt} - \frac{i\frac{dOCV}{dSOC}}{3600Q_{cell}};$$
$$L_f^2(h) = \frac{dL_f^1(h)}{dV_1} * f_1 + \frac{dL_f^1(h)}{dV_2} * f_2 + \frac{dL_f^1(h)}{dV_3} * f_3 + \frac{dL_f^1(h)}{di} * \frac{di}{dt} + \frac{dL_f^1(h)}{d\left(\frac{di}{dt}\right)} * \frac{d^2i}{dt^2} = \frac{\frac{i}{c_1} - \frac{V_1}{R_1c_1}}{R_1c_1} + \frac{\frac{i}{c_2} - \frac{V_2}{R_2c_2}}{R_2c_2} + \frac{di}{dt}\left(-\frac{1}{c_1} - \frac{1}{c_2} - \frac{\frac{dOCV}{dSOC}}{3600Q_{cell}}\right) - R_0\frac{d^2i}{dt^2} + \frac{i^2\frac{d^2OCV}{dSOC^2}}{\left(3600Q_{cell}\right)^2}; \quad \text{Eq. (14)}$$

The resulting observability matrix $\mathcal{O}_{3\times3}$ is derived as follows:

$$\mathcal{O} = \begin{bmatrix} \frac{dOCV}{dSOC} & -1 & -1 \\ \frac{-i\frac{d^2OCV}{dSOC^2}}{3600Q_{cell}} & \frac{1}{R_1C_1} & \frac{1}{R_2C_2} \\ \frac{-\frac{di}{dt}\frac{d^2OCV}{dSOC^2}}{3600Q_{cell}} + \frac{i^2\frac{d^3OCV}{dSOC^3}}{\left(3600Q_{cell}\right)^2} & -\frac{1}{\left(R_1C_1\right)^2} & -\frac{1}{\left(R_2C_2\right)^2} \end{bmatrix} \quad \text{Eq. (15)}$$

The measure of the system observability can be quantified with the condition number κ of the observability matrix, which is given as [29]:

$$\kappa(\mathcal{O}) = \| \mathcal{O}^{-1} \| \| \mathcal{O} \| \quad \text{Eq. (16)}$$

where $\| \cdot \|$ is the largest singular value of the matrix (calculated with svd function in MATLAB in this work).

Given that the nature of R_1, R_2, C_1, C_2, OCV, and Q_{cell} are functions of current, SOC, and temperature, input current and temperature impact the observability matrix $\mathcal{O}$.

First, the ECM observability dependence on input current i is evaluated. Different input currents (1C, 1.5C, and 2C) are employed for the ECM. The voltage profiles versus SOC with 1C, 1.5C, and 2C discharge are shown in Figure 9(a). The condition number κ in logarithmic scale ($\log_{10}$) at these discharge C-rates is plotted in Figure 9(b). The condition number is noted to rise as the current magnitude decreases. This result indicates that the ECM observability can be improved with a higher C-rate.

Further, we explore the impact of temperature on ECM observability. The 1C discharge voltage profiles versus SOC at 10°C, 25°C, and 45°C are utilized in the second-order ECM condition number as shown in Figure 10(a). The condition number κ in logarithmic scale at these temperatures is depicted in Figure 10(b). Since the OCV and RC parameters are considered as a function of temperatures, the condition number varies at different temperatures. At a low SOC range (<0.2), the condition number at 45°C is higher than that at 25°C and 10°C. When the SOC reaches 0.9–1, the condition number at 10°C becomes the largest among the three temperatures.

Across the middle SOC range (0.2–0.9), the condition numbers at these temperatures overlap. This is caused by the nonlinear coupling between the ECM parameters and temperatures.

As seen from the observability matrix in Equation 15, the gradient of OCV with respect to SOC ($dOCV/dSOC$) is a crucial metric of system observability. Since the OCV–SOC of the LFP is flat, a small noise on the OCV will lead to significant $dOCV/dSOC$ variations and potentially cause large SOC estimation errors.

FIGURE 9 Voltage response with 1C, 1.5C, and 2C discharge current at 25°C (a). The observability matrix condition number (b).

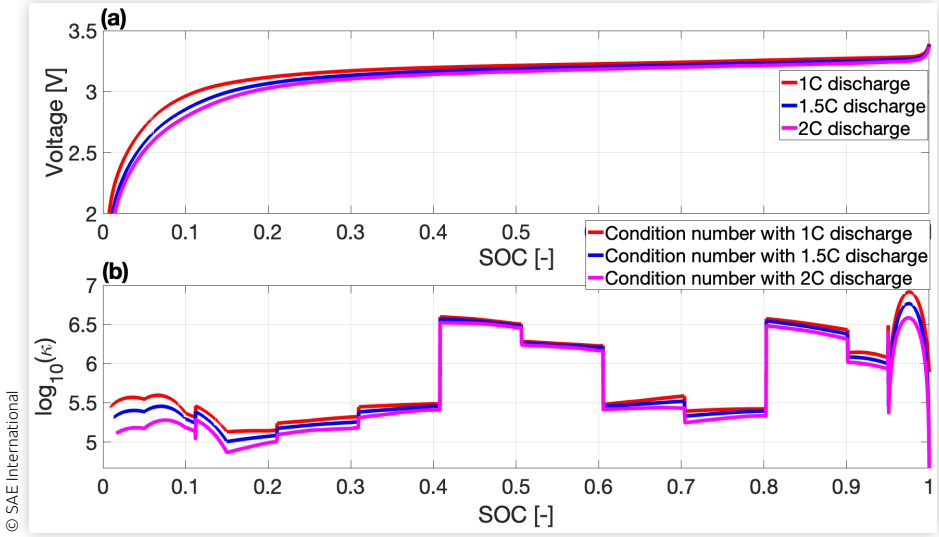

3.3. Impact of OCV Flatness on Estimator Design with Signal-to-Noise Ratio

The OCV slope with respect to SOC $(dOCV/dSOC)_n$ is defined as:

$$\left(\frac{dOCV}{dSOC}\right)_n = \frac{OCV_{n+1} - OCV_n}{SOC_{n+1} - SOC_n} \qquad \text{Eq. (17)}$$

where *OCV* and *SOC* are stored as vectors; OCV_n and SOC_n are the *n*th value in the *OCV* and *SOC* vectors.

To further quantify the impact of the OCV flatness on the ECM observability, the SNR is adopted. In this context, we assume the presence of white Gaussian noise with a mean value of 1 mV added to the OCV. The resulting SNR_{OCV} is calculated as 55 dB using Equation 1, as illustrated in Figure 11. The choice of noise with a mean value of 1 mV is deliberate, as this value aligns with the typical accuracy ranges of voltage sensors used in BMSs and battery voltage prediction models. The resulting *dOCV/dSOC* with added noise is plotted in Figure 11(b). As depicted in Equation 15, the *dOCV/dSOC* plays a crucial role in the observability matrix. Any change in the *dOCV/dSOC* results in a corresponding alteration in the

FIGURE 10 Voltage response with 1C discharge current at 10°C, 25°C, and 45°C (a). The observability matrix condition number (b).

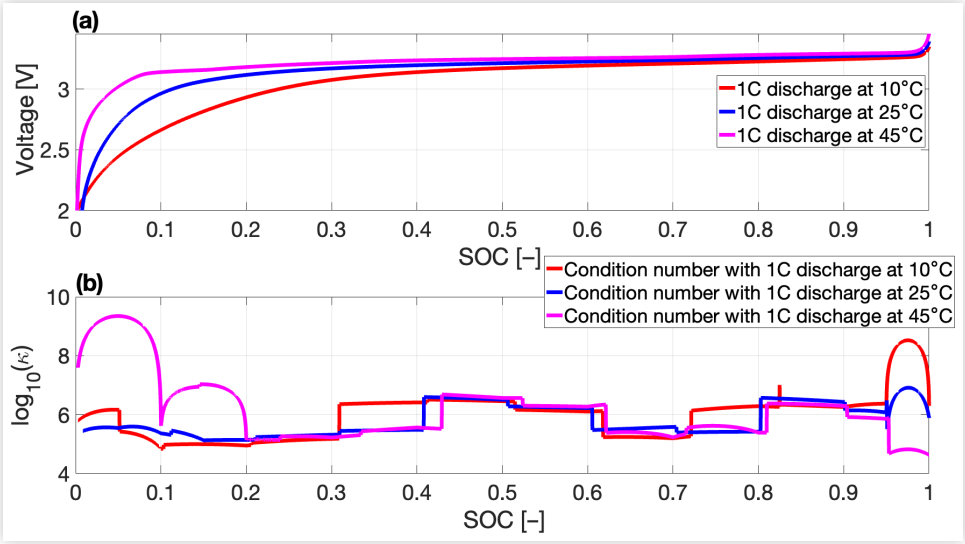

FIGURE 11 OCV and OCV with added white Gaussian noise (noise mean value = 1 mV, SNR_{OCV} = 55 dB) (a); *dOCV/dSOC* and *dOCV/dSOC* with added white Gaussian noise (noise mean value = 1 mV, SNR_{OCV} = 55 dB) (b).

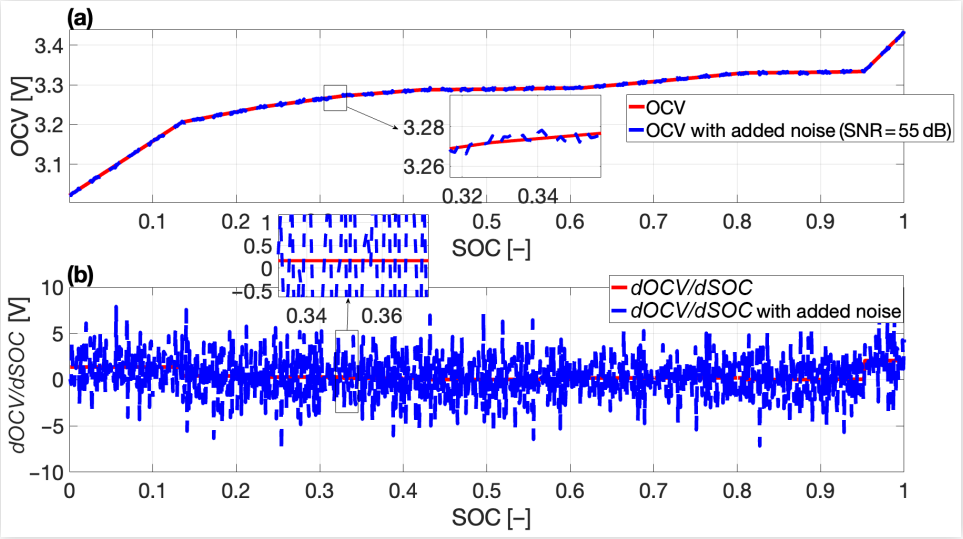

observability matrix. Furthermore, the condition number κ, computed using Equation 19, relies on the observability matrix. Therefore, it is important to explore the influence of OCV flatness on both *dOCV/dSOC* and the condition number, especially under conditions of SNR variations caused by the introduction of noise to the OCV.

The SNR, in decibels, of (*dOCV/dSOC*) vector is computed as the ratio of its summed squared magnitude to that of the added noise vector *noise*:

$$SNR_{dOCV/dSOC}\left(dOCV/dSOC, noise\right) = 20\log_{10}\left(\sqrt{\frac{\Sigma_{n=1}^{N}\left|\left(dOCV/dSOC\right)_n\right|^2}{\sqrt{\Sigma_{n=1}^{N}\left|noise_n\right|^2}}}\right) \quad \text{Eq. (18)}$$

Also, the *SNR* of condition number κ in the observability matrix can be calculated as:

$$SNR_{\kappa}\left(\kappa, noise\right) = 20\log_{10}\left(\frac{\sqrt{\Sigma_{n=1}^{N}\left|\kappa_n\right|^2}}{\sqrt{\Sigma_{n=1}^{N}\left|noise_n\right|^2}}\right) \quad \text{Eq. (19)}$$

where N is the length of the condition number κ vector; κ_n is the nth κ vector.

The OCV is pivotal in the SOC estimation using the OCV–SOC lookup table method. To measure the resilience of SOC estimation employing the OCV–SOC lookup table against OCV flatness, the SNR of the SOC estimation solely based on the OCV–SOC lookup table is evaluated in the presence of small noise added to the OCV. Similarly, the SNR for SOC estimation utilizing only the OCV–SOC lookup table is expressed as follows:

$$SNR_{\widehat{SOC}_{look-up-table}}\left(\widehat{SOC}_{look-up-table}, noise\right) = 20\log_{10}\left(\frac{\sqrt{\Sigma_{n=1}^{N}\left|\widehat{SOC}_{look-up-table_n}\right|^2}}{\sqrt{\Sigma_{n=1}^{N}\left|noise_n\right|^2}}\right) \quad \text{Eq. (20)}$$

where N is the length of $\widehat{SOC}_{look-up-table}$ vector estimated only with the OCV–SOC lookup table method; $\widehat{SOC}_{look-up-table_n}$ is the nth $\widehat{SOC}_{look-up-table}$ vector.

The SNR results of *dOCV/dSOC* with Equation 18 are depicted in Figure 12. It can be noted that the SNR of *dOCV/dSOC* decreases below 0 dB, even when 55 dB noise is added to the OCV. On the logarithmic scale, the negative SNR means the signal level is smaller than the noise level and it is difficult to distinguish the desired signal from the noise. This result illustrates that even if a minor noise (noise mean value = 1 mV, SNR_{OCV} = 55 dB) is introduced to the OCV signal, the prediction error of *dOCV/dSOC* caused by the noise will increase vastly. The SNR decay also signifies the impact of OCV flatness on the SOC estimator. Specifically, for the SOC range of 0.4–0.6 and 0.8–0.9, the SNR drops to –25 dB. This indicates that the *dOCV/dSOC* at these regions is most sensitive to uncertainty and can lead to the most significant estimation errors. Also, this means that the robustness of the ECM could be better in these regions.

Since *dOCV/dSOC* is an essential term in the system observability matrix, as shown in Equation 15, a slight noise would inevitably impact the ECM observability and increase the opportunity of losing the rank of the observability matrix. Furthermore, the SNR of the condition number κ in the observability matrix after the OCV noise

FIGURE 12 SNR of *dOCV/dSOC* ($SNR_{dOCV/dSOC}$) after white Gaussian noise is added to the OCV (noise mean value = 1 mV) at different SOC ranges.

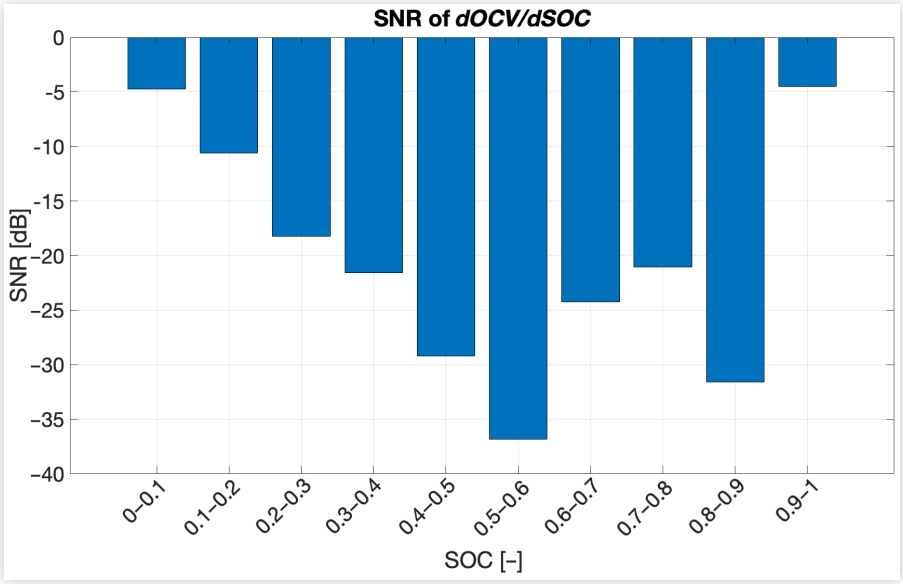

is added is shown in Figure 13. It can be observed that the SNR is below 30 dB across the entire SOC range. Similarly, the relatively lower SNR regions are SOC ranges of 0.4–0.6 and 0.8–0.9. This finding also verifies that the ECM observability within these SOC regions is most susceptible to OCV noise. Therefore, it can be inferred that the effect of the OCV flatness of LFP batteries on ECM observability can be quantified with SNR.

Lastly, the SNR of the SOC estimation with only the SOC–OCV lookup table after the OCV noise is added is shown in Figure 14. All the SNRs calculated with Equation 20 decrease below 40 dB. In addition, the SNR of SOC regions of 0.4–0.6 and 0.8–0.9 remain the lowest. This result illustrates that the LFP OCV noise with a mean value of 1 mV will lead to large SOC estimation errors with only the OCV–SOC lookup table and the largest SOC estimation errors appear in the SOC ranges of 0.4–0.6 and 0.8–0.9.

To sum up, the SNR can analyze the impact of the LFP OCV on ECM observability and SOC estimation with the OCV–SOC lookup table method. The most susceptible SOC regions, due to OCV flatness, can be positioned with the lowest SNR values.

FIGURE 13 SNR of observability matrix condition number (SNR_{κ}) after white Gaussian noise is added to the OCV (noise mean value = 1 mV) at different SOC ranges.

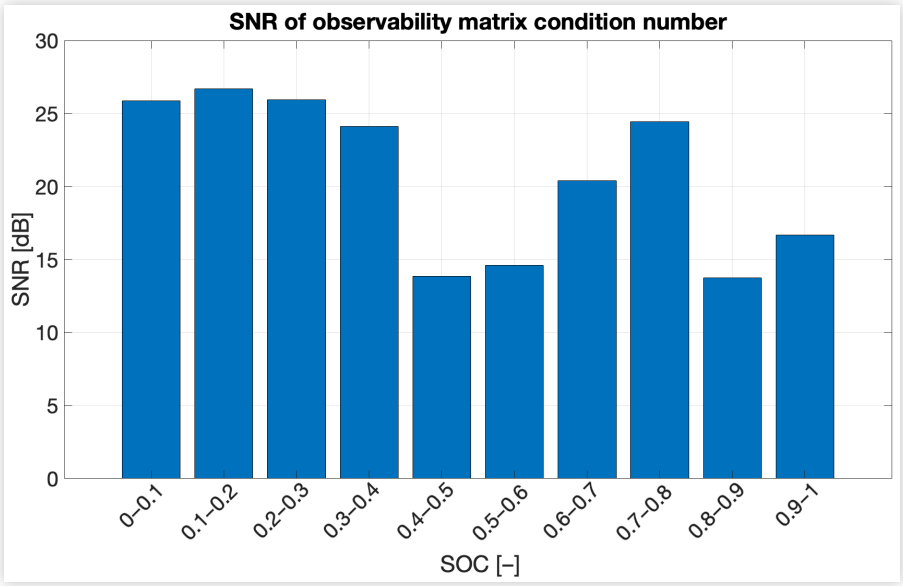

FIGURE 14 SNR of SOC estimation only with SOC–OCV lookup table $\left(SNR_{\widehat{SOC}_{look-up-table}}\right)$ after white Gaussian noise is added to the OCV (noise mean value = 1 mV) at different SOC ranges.

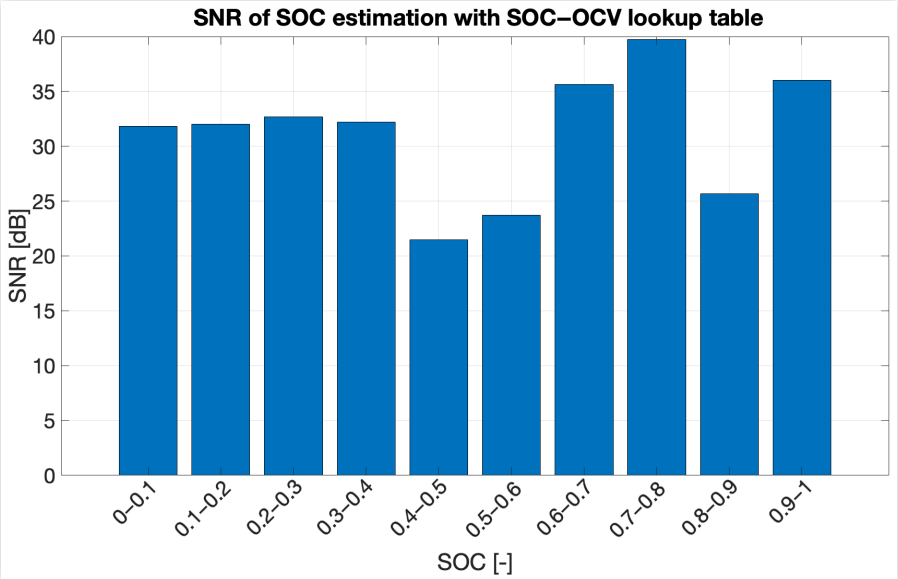

4. SOC Estimator Design, Robustness Analysis, and Implementation with Aircraft Usage Profiles

In this section, the ECM-based EKF and UKF are developed for SOC estimation. The robustness of the SOC estimator against input noise is analyzed. The SOC estimator sensitivity with different process covariances Q and measurement noise covariances R are investigated. The aircraft usage profiles are used to evaluate the effectiveness of the SOC estimator.

4.1. Observer Design with ECM

The discrete-time state-space of the ECM in Equation 9 is given as [48]:

$$\underbrace{\begin{bmatrix} V_{1,k+1} \\ V_{2,k+1} \\ SOC_{k+1} \end{bmatrix}}_{x_{k+1}} = \underbrace{\begin{bmatrix} \frac{-T_s}{e^{R_1C_1}} & 0 & 0 \\ 0 & \frac{-T_s}{e^{R_2C_2}} & 0 \\ 0 & 0 & 1 \end{bmatrix}}_{A_k} \underbrace{\begin{bmatrix} V_{1,k} \\ V_{2,k} \\ SOC_k \end{bmatrix}}_{x_k} + \underbrace{\begin{bmatrix} R_1 * \left(1 - e^{\frac{-T_s}{R_1C_1}}\right) \\ R_2 * \left(1 - e^{\frac{-T_s}{R_2C_2}}\right) \\ \frac{T_s}{3600 * Q_{cell}} \end{bmatrix}}_{B_k}$$

$$i_k = f\left(x_k, i_k\right)_{3\times 1} \qquad \text{Eq. (21)}$$

$$V_k = OCV\left(SOC_k, T\right) - V_{1,k} - V_{2,k} - R_0 * i_k = h\left(x_k, i_k\right) \qquad \text{Eq. (22)}$$

To implement the EKF, the ECM state-space function must be linearized using the Taylor series around the present estimated state $\hat{x}_k$ at time step k. The calculation process of the Jacobian matrix of ECM is given as [48]:

$$F_d = \frac{\partial f\left(x_k, i_k\right)}{\partial x_k}\Big|_{x_k=\hat{x}_k} \qquad \text{Eq. (23)}$$

$$= \begin{bmatrix} \frac{\partial f_1\left(x_k,i_k\right)}{\partial V_1} & \frac{\partial f_1\left(x_k,i_k\right)}{\partial V_2} & \frac{\partial f_1\left(x_k,i_k\right)}{\partial SOC} \\ \frac{\partial f_2\left(x_k,i_k\right)}{\partial V_1} & \frac{\partial f_2\left(x_k,i_k\right)}{\partial V_2} & \frac{\partial f_2\left(x_k,i_k\right)}{\partial SOC} \\ \frac{\partial f_3\left(x_k,i_k\right)}{\partial V_1} & \frac{\partial f_3\left(x_k,i_k\right)}{\partial V_2} & \frac{\partial f_3\left(x_k,i_k\right)}{\partial SOC} \end{bmatrix}_{x_k=\hat{x}_k}$$

$$= \begin{bmatrix} e^{\frac{-T_s}{R_1C_1}} & 0 & 0 \\ 0 & e^{\frac{-T_s}{R_2C_2}} & 0 \\ 0 & 0 & 1 \end{bmatrix}_{x_k=\hat{x}_k} \qquad \text{Eq. (24)}$$

$$H_d = \frac{\partial h\left(x_k, i_k\right)}{\partial x_k}\Big|_{x_k=\hat{x}_k^+}$$

$$= \begin{bmatrix} \frac{\partial h\left(x_k,i_k\right)}{\partial V_1} & \frac{\partial h\left(x_k,i_k\right)}{\partial V_2} & \frac{\partial h\left(x_k,i_k\right)}{\partial SOC} \end{bmatrix}_{x_k=\hat{x}_k}$$

$$= \left[-1 \; -1 \; \frac{\partial OCV\left(SOC_k\right)}{\partial SOC}\right]_{x_k=\hat{x}_k}$$

TABLE 3 Algorithm: EKF.

1 **Input:** $\hat{x}(0|0)$, $\hat{P}(0|0)$, $Q_{3\times3}$, $R_{1\times1}$
2 **Output**: $\hat{x}(k+1|k+1)$, $\hat{P}(k+1|k+1)$
3 **Require:** Initialization of state and error covariance matrix.
4 State estimate at time step 0: $\hat{x}(0|0)$. $\hat{x}$ represents the estimated states. $x=[V_1, V_2, SOC]$. State estimation error covariance matrix at time step 0: $\hat{P}(0|0)$.
5 **For** time step k=1,2,….**do**
6 Priori state estimation:
$\hat{x}(k+1|k) = f(\hat{x}(k|k), i)$
7 Project the error covariance ahead:
$\hat{P}(k+1|k) = F_d^T(k) + \hat{P}(k|k)F_d^T(k) + Q$
Q is the covariance of the process noise.
8 Compute the Kalman filter gain:
$K(k+1) = \hat{P}(k+1|k)H_d^T(k)\left(H_d(k)\hat{P}(k+1|k)H_d^T(k) + R\right)^{-1}$
R is the covariance of the measurement noise.
9 Update the estimate with the error V_{error} between measurement model prediciton:
$\hat{x}(k+1|k+1) = \hat{x}(k+1|k) + K(k+1)(V_{error})$
10 Update the covariance of the state variables:
$\hat{P}(k+1|k+1) = (I - K(k+1)H_d\hat{P}(k+1|k)$
11 **end for**

where $\boldsymbol{F_d}$ is the discrete-time Jacobian matrix of ECM; T_s is the discrete sample time; $\boldsymbol{H_d}$ is the discrete-time derivative of the voltage output equation on state vector; $f_1(x_k, i_k)$, $f_2(x_k, i_k)$, and $f_3(x_k, i_k)$ are the first, second, and third row of $f(x_k, i_k)$, respectively. The EKF algorithm calculation process comprises initialization, prediction, and correction, as shown in the pseudo-code (Table 3).

The UKF follows the steps described in Table 4.

4.2. Observer Robustness against Input Noise

To assess the influence of SNR within various *dOCV/dSOC* intervals on the state estimator, the EKF and UKF, coupled with the second-order ECM, are applied to GITT data. Biased voltage measurements are generated by introducing random noise to the recorded voltage measurements. The referenced SOC is calculated using the Coulomb counting. The implementation processes of EKF and UKF are widely reported in the literature and are not repeated in this article. Interested readers could refer to the references for more introduction [42]. Consider that voltage measurements with an SNR of 55 dB are added to the EKF based on second-order ECM. The voltage estimation and estimation errors are plotted in Figure 15(a) and (b). In Figure 15(a) and (b), the

TABLE 4 Algorithm: UKF.

1 **Input:** $\hat{x}(0|0)$, $\hat{P}(0|0)$, $Q_{3\times3}$, $R_{1\times1}$
2 **Output**: $\hat{x}(k+1|k+1)$, $\hat{P}(k+1|k+1)$
3 **Require:** Initialization of state and error covariance matrix.
4 State estimate at time step 0: $\hat{x}(0|0)$. $\hat{x}$ represents the estimated states. $x=[V_1, V_2, SOC]$. State estimation error covariance matrix at time step 0: $\hat{P}(0|0)$.
5 **For** time step k=1,2,….**do**
6 Choose the sigma points $x^i(k|k)$:

$$x^i(k|k) = \begin{cases} \hat{x}(k+1|k), i=1 \\ \hat{x}(k+1|k) + \left(\sqrt{(n+\lambda)\hat{P}(k|k)}\right)_i, i=2,\dots n+1 \\ \hat{x}(k+1|k) - \left(\sqrt{(n+\lambda)\hat{P}(k|k)}\right)_i, i=n+2,\dots,2n+1 \end{cases}$$

$$W_m^{(i)} = \begin{cases} \frac{\lambda}{n+\lambda}, i=1 \\ \frac{1}{2(n+\lambda)}, i\neq 1 \end{cases}$$

$$W_c^{(i)} = \begin{cases} \frac{\lambda}{n+\lambda} + (1-\alpha^2+\beta), i=1 \\ \frac{1}{2(n+\lambda)}, i\neq 1 \end{cases}$$

$x \in R^n$. $\lambda = \alpha^2(n+\kappa) - n, \alpha\epsilon[0,1]$. n=3 in this paper. $W_m^{(i)}$ and $W_c^{(i)}$ are mean and variance of the x, respectively.
7 Priori state estimation:
$\hat{x}(k+1|k) = \sum_{i=1}^{2n+1} W_m^{(i)} \hat{x}^i(k+1|k)$
8 Project the error covariance ahead:
$\hat{P}(k+1|k) = \sum_{i=1}^{2n+1} W_m^{(i)} (\hat{x}^i(k+1|k) - \hat{x}(k+1|k))((\hat{x}^i(k+1|k) - \hat{x}(k+1|k))^T + Q$
Q is the covariance of the process noise.
9 Estimate the output voltage:
$\hat{V}(k+1|k) = \sum_{j=1}^{2n+1} W_m^{(j)} \hat{V}^j(k+1|k)$
10 Estimate the covariance of the measurement P_y and the covariance between the measurement and the state P_{xy}:
$P_y = \sum_{j=1}^{2n+1} W_m^{(j)} (\hat{V}^j(k+1|k) - \hat{V}(k+1|k)) \left(\hat{V}^j(k+1|k) - \hat{V}(k+1|k)\right)^T + R$
$P_{xy} = \sum_{j=1}^{2n+1} (\hat{x}^j(k+1|k) - \hat{x}(k+1|k)) \left(\hat{V}^j(k+1|k) - \hat{V}(k+1|k)\right)^T$
R is the covariance of the measurement noise.
11 Compute the Kalman filter gain:
$K(k+1) = P_{xy}P_y^{-1}$
12 Update the state estimate with the error error V_{error}between measurement model prediction.
$\hat{x}(k+1|k+1) = \hat{x}(k+1|k) + K(k+1)(V_{error})$
13 Update the covariance of the state variables:
$\hat{P}(k+1|k+1) = \hat{P}(k+1|k) - K(k+1)P_yK^T(k+1)$
14 **end for**

FIGURE 15 EKF voltage estimation with white Gaussian noise added to the voltage under GITT condition. (a) Experimental voltage vs. EKF estimated voltages with and without noise. (b) EKF voltage estimation errors with and without noise.

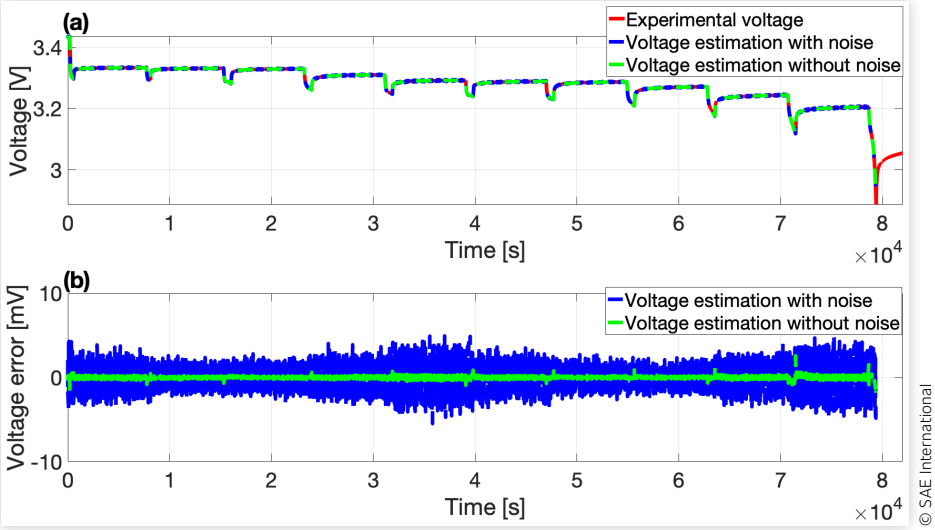

EKF with the ECM, without noise, accurately follows the measured voltage, with the corresponding estimation error staying below 2 mV. Although the voltage estimation maintains robustness after adding noise to the voltage measurement, the estimation error increases. The observability analysis verifies that the ECM is locally observable across the SOC range. Thus, it is feasible to estimate the SOC with added noise. The SOC estimation and estimation errors are shown in Figure 16(a) and (b). The EKF is established with the Taylor expansion of the ECM. Thus, the linearization of the system will increase the possibility of losing the rank of the observability matrix. Even though the voltage estimation is converged without added noise, the SOC estimation error can be found, as shown in Figure 16(a) and (b). Furthermore, the introduction of noise results in a more pronounced SOC estimation error compared to the SOC estimation outcomes without added noise. Notably, the SOC estimation error experiences the most significant increase within the SOC range of 0.4–0.6 and 0.8–0.9, as depicted in Figure 16(b). It is noteworthy that the SNR of *dOCV/dSOC* is lowest in these SOC ranges, indicating that even slight noise in these SOC regions can lead to considerable fluctuations in the *dOCV/dSOC* values.

Given the crucial role of *dOCV/dSOC* in linearizing the OCV concerning SOC, these SOC regions with low SNR exhibit large sensitivity to noise, resulting in substantial

FIGURE 16 EKF SOC estimation with white Gaussian noise added to the voltage under GITT condition. (a) Referenced SOC with Coulomb counting vs. EKF estimated SOC with/without noise. (b) EKF SOC estimation errors with and without noise.

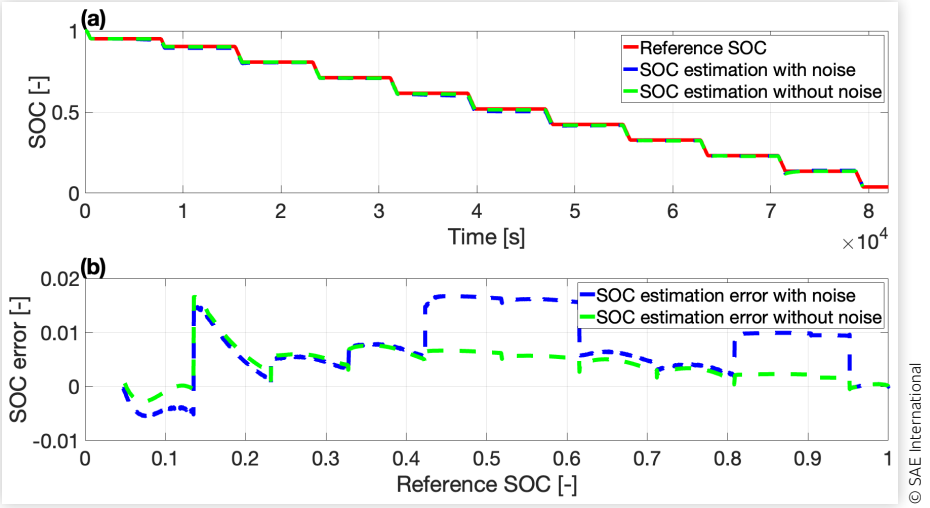

FIGURE 17 UKF voltage estimation with white Gaussian noise added to the voltage under GITT condition. (a) Experimental voltage vs. UKF estimated voltages with/without noise. (b) EKF voltage estimation errors with and without noise.

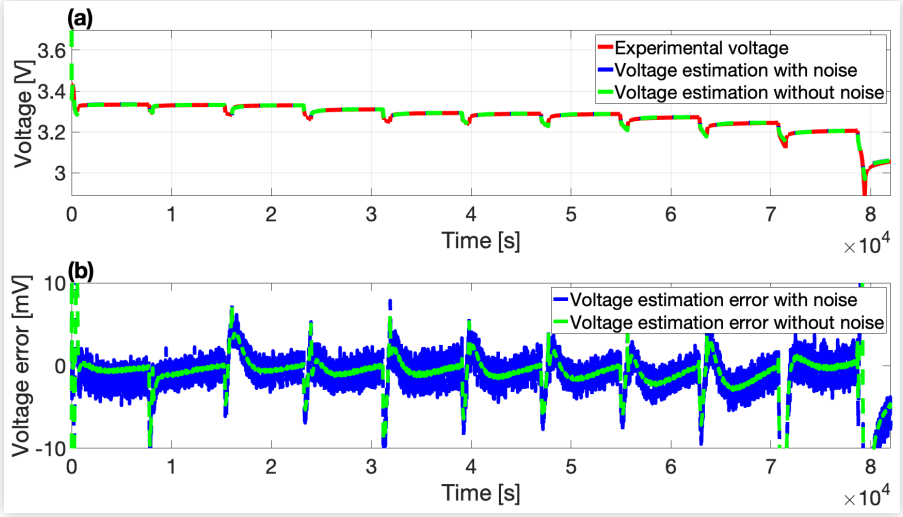

deviations of the EKF-based SOC estimation from its reference values.

The voltage estimation results with UKF using the ECM are plotted in Figure 17(a) and (b). Without the added noise, the voltage estimation remains the error below 10 mV. Similarly, the voltage noise with an SNR of 55 dB is added to the voltage measurements to investigate the UKF robustness against input noise. The added noise inevitably increases the voltage estimation errors. The SOC estimation results with UKF are summarized in Figure 18(a) and (b).

Compared with the EKF, UKF uses a sigma-point sampling technique to approximate the state variables' distribution and input noise. By selecting a set of carefully chosen sigma points (sample points) from the current state estimate, the filter effectively captures the statistical properties of the state and input variables. This allows the filter to handle non-Gaussian and nonlinear noise distributions, making it robust to various types of input noise.

As shown in Figure 18(a) and (b), it can be found that the SOC estimation with UKF could remain robust against the input noise. The SOC estimation error is below 1% even if the noise is added to the observer. Note that, unlike the EKF, no system linearization is required. Removing the linearization process leads to a computational complexity comparable between the UKF and EKF. In addition, since the *dOCV/dSOC* is no longer needed in the UKF calculation process, the low SNR of the *dOCV/dSOC* at different SOC regions will not impact the

FIGURE 18 UKF SOC estimation with white Gaussian noise added to the voltage under GITT condition. (a) Referenced SOC with Coulomb counting vs. UKF estimated SOC with/without noise. (b) UKF SOC estimation errors with and without noise.

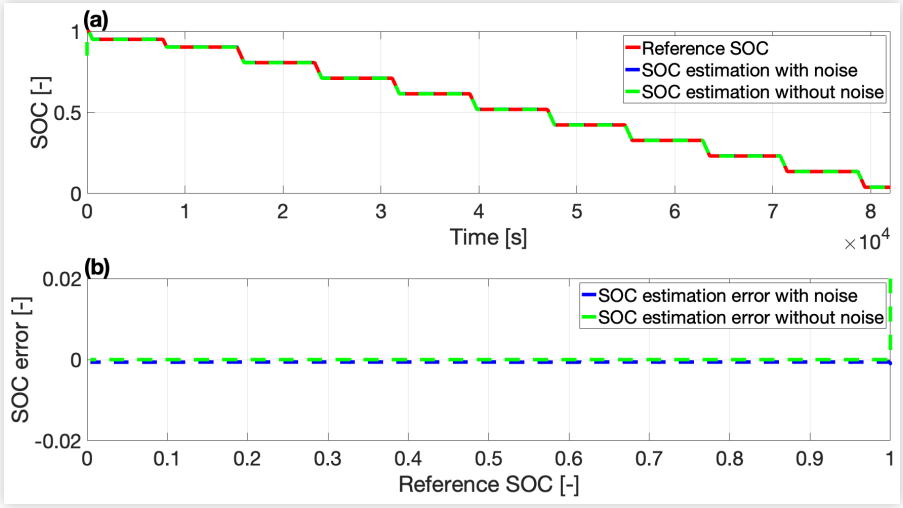

performance of the SOC estimation. Hence, the robustness of the UKF against the input noise is better than the EKF.

4.3. Observer Sensitivity

The process noise covariance matrix Q and sensor noise covariance R significantly affect the filter's performance. Therefore, they are frequently employed as tuning parameters to attain the desired filter performance. Different Q and R values are applied to the EKF and UKF with ECM. The initial Q and R for EKF and UKF are listed in Appendix C.

The voltage and SOC estimation results of EKF with different Q and R values are shown in Figure 19(a)–(h). Note that Q is a 3×3 diagonal matrix. The three parameters ($Q(1,1)$, $Q(2,2)$, and $Q(3,3)$) in Q are tuned separately to evaluate their effects on the filter. In Figure 19(a) and (b), it can be observed that increasing $Q(1,1)$ from 10^0 to 10^8 does not significantly impact the convergence rate of voltage estimation. Still, the convergence of the SOC estimation is accelerated when a large $Q(1,1)$ is applied. A high value of Q implies substantial uncertainty in predicting states solely based on the model. As a result, the accuracy of state corrections becomes heavily reliant on measurements. In these situations, convergence from an initial condition error occurs rapidly, but if Q is set too high, the estimate may become noisy. Since $Q(1,1)$ is directly relevant to the first state of the state vector x, the SOC estimation convergence could be improved with larger $Q(1,1)$ values. In Figure 19(c) and (d), selecting a larger $Q(2,2)$ can obtain a faster convergence of the voltage estimation, but a slower SOC convergence. The same result is found in Figure 19(e) and (f) for different $Q(3,3)$ values. This is because $Q(2,2)$ and $Q(3,3)$ correspond to states V_1 and V_2. More considerable modifications would be imposed on V_1 and V_2 rather than on SOC. Thus, the effects of $Q(2,2)$ and $Q(3,3)$ on EKF are opposite compared with $Q(1,1)$.

In terms of R, a larger R indicates that the measurement is uncertain and should not be trusted to make significant state corrections based on the measurements. Therefore, the state convergence could be slow. The results of EKF performances with different R values are plotted in Figure 19(g) and (h). It is evident that increasing R from 10^{-7} to 10^9 will yield a smaller convergence rate both on voltage estimation and SOC estimation. Thus, to avoid significant state corrections, Q should be decreased, or R should be increased to decrease the Kalman gain for the EKF.

For UKF with different Q and R values, the results are plotted in Figure 20(a)–(h). Increasing $Q(1,1)$ from 10^{-19} to 10^{-3}, the UKF becomes more sensitive to changes. It can help the filter better adapt to abrupt changes in the system behavior. However, if Q is set too high, it can lead

FIGURE 19 Effect of tuning the process noise covariance $Q_{3\times3}$ and sensor noise covariance R on EKF estimation error for SOC and voltage under GITT condition. (a) Different $Q(1,1)$ on voltage estimation error. (b) Different $Q(1,1)$ on SOC estimation error. (c) Different $Q(2,2)$ on voltage estimation error. (d) Different $Q(2,2)$ on SOC estimation error. (e) Different $Q(3,3)$ on voltage estimation error. (f) Different $Q(3,3)$ on SOC estimation error. (g) Different R on voltage estimation error. (h) Different R on SOC estimation error.

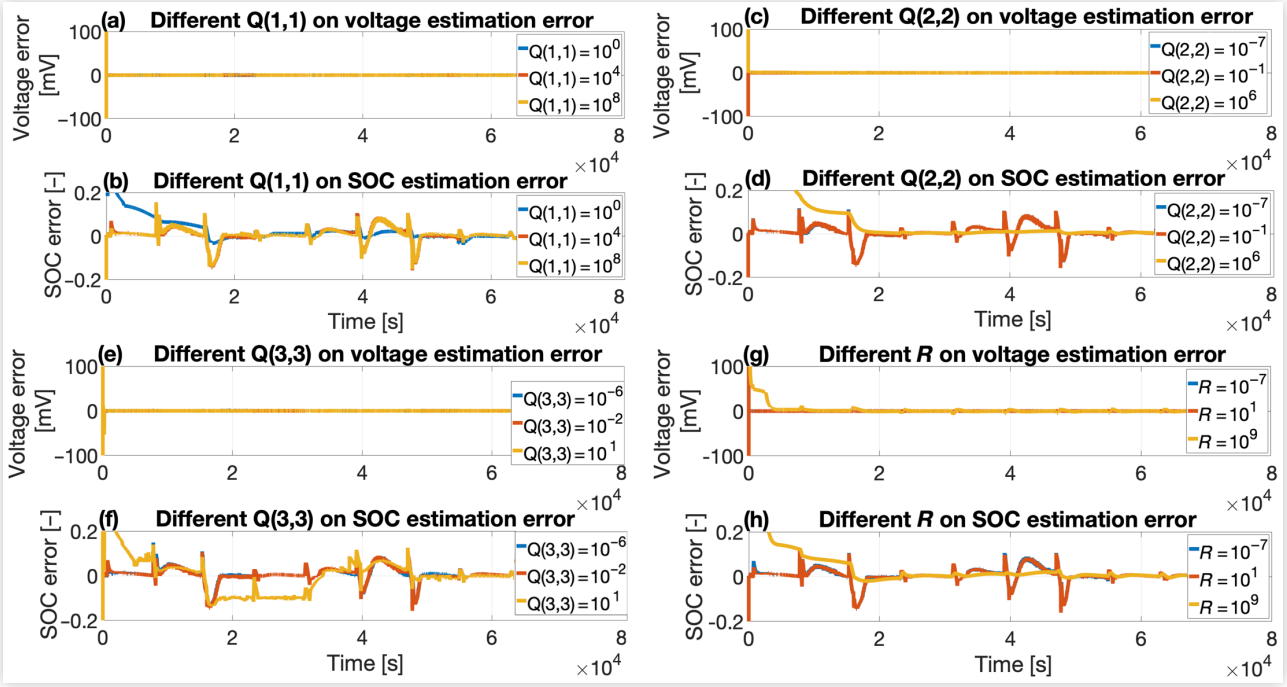

FIGURE 20 Effect of tuning the process noise covariance $Q_{3\times3}$ and sensor noise covariance R on UKF estimation error for SOC and voltage under GITT condition. (a) Different $Q(1,1)$ on voltage estimation error. (b) Different $Q(1,1)$ on SOC estimation error. (c) Different $Q(2,2)$ on voltage estimation error. (d) Different $Q(2,2)$ on SOC estimation error. (e) Different $Q(3,3)$ on voltage estimation error. (f) Different $Q(3,3)$ on SOC estimation error. (g) Different R on voltage estimation error. (h) Different R on SOC estimation error.

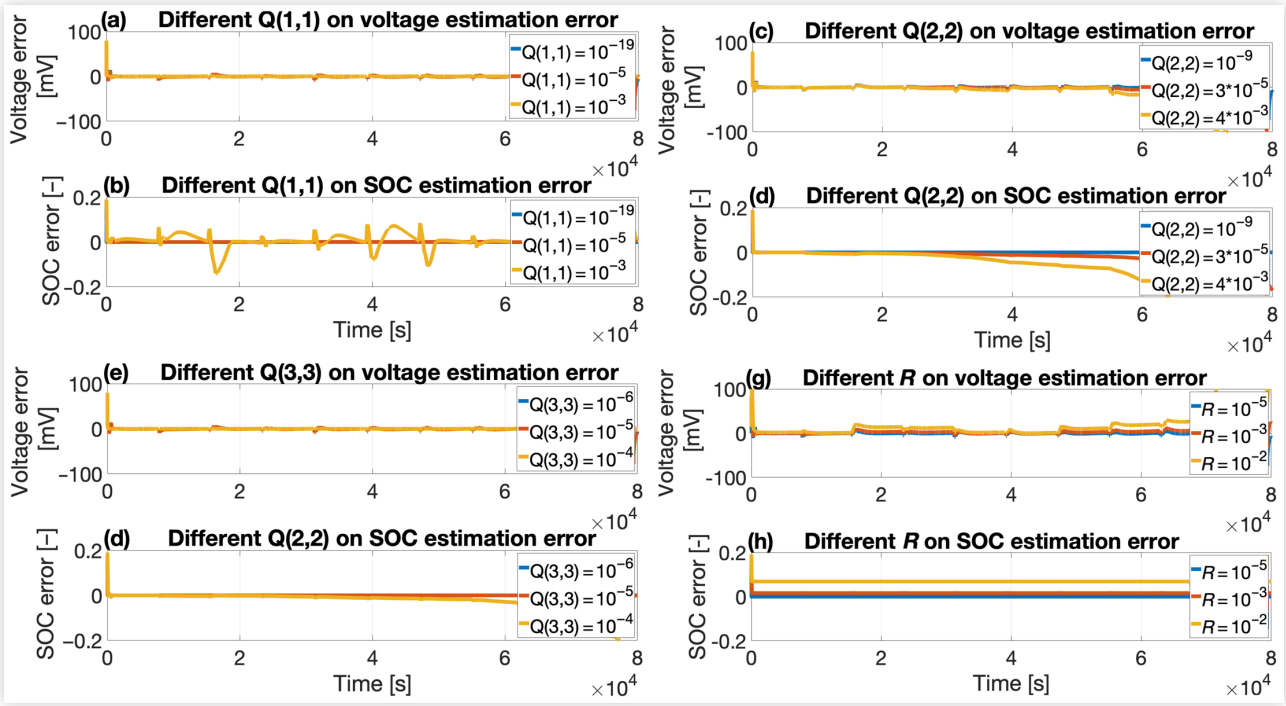

to overfitting and decreased tracking accuracy as shown in Figure 20(a) and (b). A lower process noise covariance will make the UKF more conservative and rely more on the state transition model. This can result in smoother state estimates, which might be desirable when dealing with noisy measurements or when the actual process is relatively stable. It can be seen from Figure 20(c)–(f). When $Q(2,2)$ and $Q(3,3)$ are increased to 4×10^{-5} and 10^4, respectively, the SOC and voltage estimations could converge quickly. Still, they could not maintain stability in the final stages of the estimates. Choosing the appropriate Q is often a trade-off between tracking accuracy and robustness. A trade-off must be considered to ensure that the filter can adapt to changes in the system while not being overly sensitive to noise or disturbances. For R in Figure 20(g) and (h), it is seen that a larger R of 10^{-2} will lower the convergence of the state estimations.

4.4. SOC Estimation with Experimental Data of Aircraft Usage Profiles

We investigate the performance of the proposed UKF estimator for different aircraft usage profiles. The design principle and parameters of these three scenarios (S1, S2, and S3) are elaborated in Section 2. The experimental current and voltage data of S1, S2, and S3 are shown in Figure 21(a)–(f). The UKF estimator is evaluated with experimental data of the three aircraft usage profiles at different temperatures (10°C, 25°C, and 45°C). The UKF with ECM at 10°C, 25°C, and 45°C are shown in Figure 22. The UKF with ECM estimation errors at 10°C, 25°C, and 45°C are shown in Figure 23. An initial SOC error of 0.5 is given in the UKF. In Figure 23(a) and (b), the voltage estimation error at S1 quickly decreases to 2 mV and the SOC estimation error drops to 1% within 5 s. The average error of the voltage estimation is 11.1 mV, and the RMSE of the SOC estimation is 1.66%. At S2, the average error of the voltage estimation is 9.9 mV, and the RMSE of the SOC estimation is 1.27%. Also, the average error of the voltage estimation at S3 is 1.6 mV, and the RMSE of the SOC estimation at S3 is 1.21%. Figure 22 also summarizes the results of UKF estimation at 10°C, 25°C, and 45°C. It can be found that the voltage estimation and SOC estimation could remain robust with three scenarios. In Figure 23(a) and (b), the voltage estimation at S1 has an average error of 5.2 mV and the SOC estimation achieves an RMSE of 0.85%. For estimation results at S2 in Figure 23(c) and (d), the average error of voltage estimation is 6.4 mV and the RMSE of the SOC estimation is 1.13%. At S3, the average error of voltage estimation is 2.9 mV and the RMSE of the SOC estimation is 0.55%. Finally, the voltage and SOC estimation results with UKF at 45°C are plotted

FIGURE 21 (a) Experimental current profile of S1 and temperatures are 10°C, 25°C, and 45°C. (b) Experimental voltage response of S1 and temperatures are 10°C, 25°C, and 45°C. (c) Experimental current profile of S2 and temperatures are 10°C, 25°C, and 45°C. (d) Experimental voltage response of S2 and temperatures are 10°C, 25°C, and 45°C. (e) Experimental current profile of S3 and temperatures are 10°C, 25°C, and 45°C. (f) Experimental voltage response of S3 and temperatures are 10°C, 25°C, and 45°C.

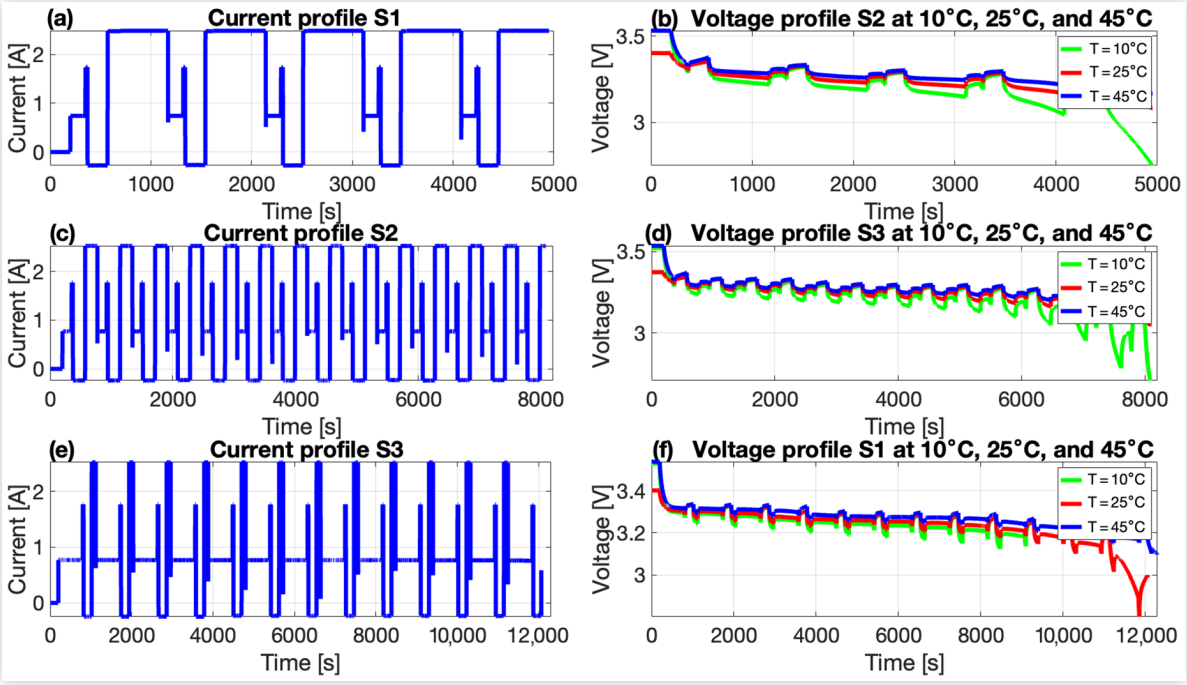

FIGURE 22 Voltage and SOC estimations from UKF under S1, S2, and S3, and the temperatures are 10°C, 25°C, and 45°C. (a) Voltage estimation of S1. (b) SOC estimation of S1. (c) Voltage estimation of S2. (d) SOC estimation of S2. (e) Voltage estimation of S3. (f) SOC estimation of S3.

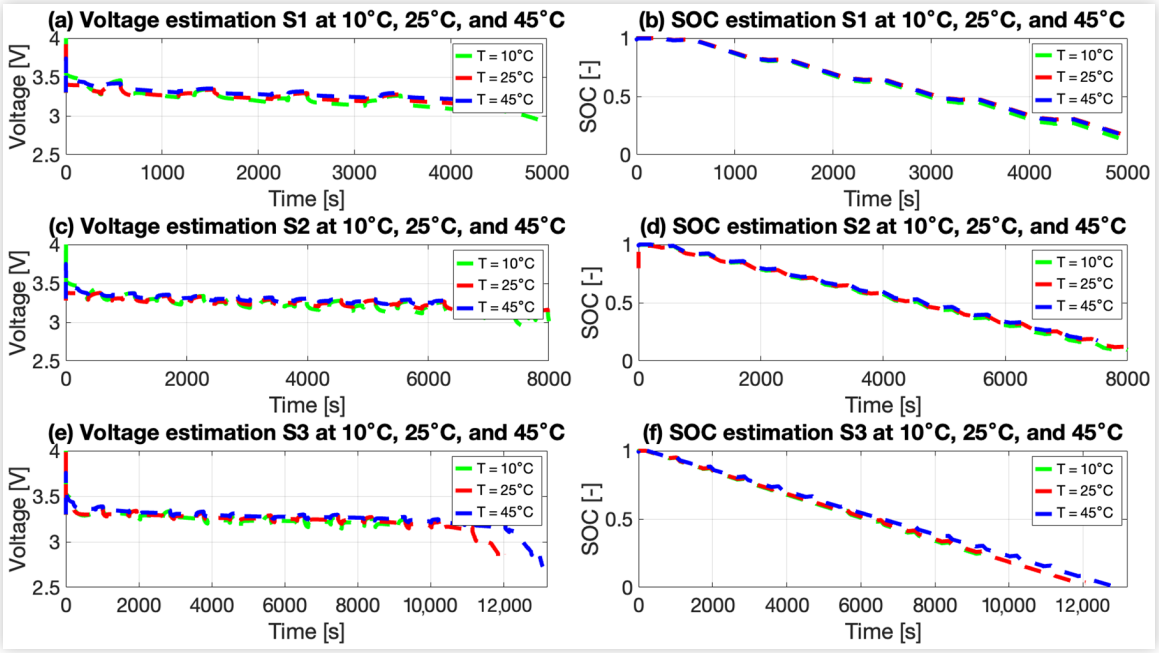

FIGURE 23 Voltage and SOC estimation errors from UKF under S1, S2, and S3, and the temperatures are 10°C, 25°C, and 45°C. (a) Voltage estimation error of S1. (b) SOC estimation error of S1. (c) Voltage estimation error of S2. (d) SOC estimation error of S2. (e) Voltage estimation error of S3. (f) SOC estimation error of S3.

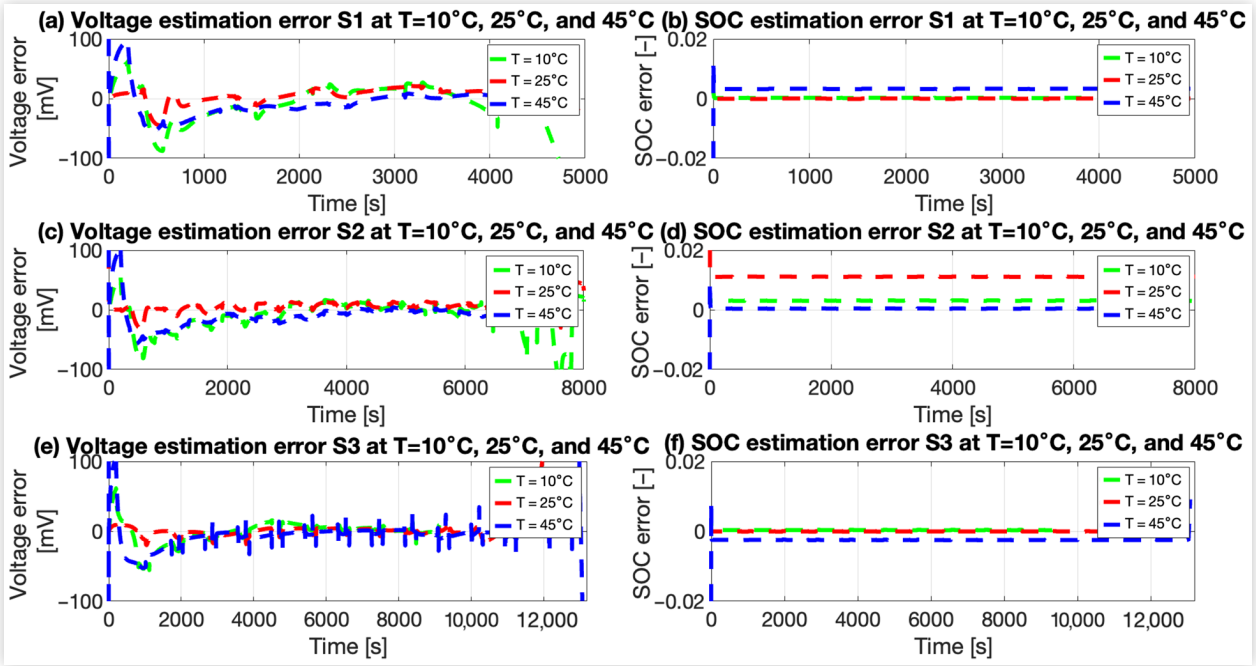

in Figure 22. The UKF estimations at 45°C achieve agreeable accuracy across three scenarios. As shown in Figure 23(a) and (b), the average error of the voltage estimation is 5.8 mV, and the RMSE of the SOC estimation is 0.74%. At S2, as depicted in Figure 23(c) and (d), the average error of voltage estimation is 9.1 mV, and the RMSE of the SOC estimation becomes 0.56%. For S3 in Figure 23(e) and (f), the average error of the voltage estimation is 3.6 mV and the RMSE of the SOC estimation is 0.50%. From the above analysis, it can be concluded that the UKF estimation based on the ECM could remain highly accurate with aircraft applications.

5. Conclusion

This study presents a SOC estimation scheme for a 28 V LFP aviation battery using a second-order ECM. RC parameters of ECM were accurately identified across various SOC values, temperatures, and C-rates. Nonlinear observability analysis with Lie derivatives confirmed the local observability of the model. The impact of OCV flatness on EKF robustness was assessed by analyzing the SNR changes of *dOCV/dSOC*, condition numbers, and SOC estimations using an OCV–SOC lookup table with added noise. Results indicated that SOC estimation is most sensitive to input noise in the 0.5–0.6 and 0.8–0.9 SOC ranges. EKF and UKF were applied to the model for SOC estimation under aviation duty cycles, revealing that the accuracy of EKF was significantly influenced by *dOCV/dSOC*, while UKF demonstrated superior performance. Sensitivity analysis of different Q and R values showed that increasing R values' reduced convergence rates for both EKF and UKF. For EKF, higher $Q(1,1)$ values accelerated SOC estimation convergence, while higher $Q(2,2)$ and $Q(3,3)$ values improved voltage convergence but slowed SOC convergence. For UKF, higher Q values enhanced both voltage and SOC estimation convergence. The second-order ECM with UKF is tested using experimentally designed aircraft usage profiles, showing that the SOC estimation RMSEs at three different temperatures are below 2%, illustrating the effectiveness of the UKF SOC estimation scheme for aviation batteries.

Contact Information

Yizhao Gao
yizhaog@stanford.edu

Simona Onori
sonori@stanford.edu

References

1. Brown, A. and Harris, W.L., "Vehicle Design and Optimization Model for Urban Air Mobility," *Journal of Aircraft* 57, no. 6 (2020): 1003-1013.
2. Deng, H. and Aifantis, K. E., "Applications of Lithium Batteries," in Kumar, R., Aifantis, K., and Hu, P. (eds.), *Rechargeable Ion Batteries* (2023), 83-103, Wiley, https://onlinelibrary.wiley.com/doi/abs/10.1002/9783527836703.ch4.
3. Marduand, Y., "Can Electric Aircraft Fly Meaningful Distances with Today's Technology?," 2024, accessed February 6, 2024, https://www.revolution.aero/deep_dive/betting-on-now-can-electricaircraft-fly-meaningful-distances-with-todays-technology/.
4. Fallah, N. and Fitzpatrick, C., "Is Shifting from Li-Ion NMC to LFP in EVs Beneficial for Second-Life Storages in Electricity Markets?" *Journal of Energy Storage* 68 (2023): 107740.
5. Liu, K. et al., "Transfer Learning for Battery Smarter State Estimation and Ageing Prognostics: Recent Progress, Challenges, and Prospects," *Advances in Applied Energy* 9 (2022): 100117.
6. Chen, L., Yu, W., Cheng, G., and Wang, J., "State-of-Charge Estimation of Lithium-Ion Batteries Based on Fractional-Order Modeling and Adaptive Square-Root Cubature Kalman Filter," *Energy* 271 (2023): 127007.
7. Manoharan, D., Sooriamoorthy, K.B., and Aparow, V.R., "Electric Vehicle Battery Pack State of Charge Estimation Using Parallel Artificial Neural Networks," *Journal of Energy Storage* 72 (2023): 108333.
8. De Angelis, A., Carbone, P., Santoni, F., Vitelli, M. et al., "On the Usage of Battery Equivalent Series Resistance for Shuntless Coulomb Counting and SOC Estimation," *Batteries* 9, no. 6 (2023): 286.
9. Che, Y., Xu, L., Teodorescu, R., Hu, X. et al., "Efficient State of Charge Correction for LFP Batteries Using Machine Learning Pipeline in Short-Term Voltage Relaxation," *ACS Energy Letters* (2024).
10. Beelen, H., Bergveld, H.J., and Donkers, M.C.F., "Joint Estimation of Battery Parameters and State of Charge Using an Extended Kalman Filter: A Single-Parameter Tuning Approach," *IEEE Transactions on Control Systems Technology* 29, no. 3 (2021): 1087-1101, doi:https://doi.org/10.1109/tcst.2020.2992523.
11. Takyi-Aninakwa, P., Wang, S., Zhang, H., Li, H. et al., "An Optimized Relevant Long Short-Term Memory-Squared Gain Extended Kalman Filter for the State of Charge Estimation of Lithium-Ion Batteries," *Energy* 260 (2022): 125093.
12. Liu, X., Li, Q., Wang, L., Lin, M. et al., "Data-Driven State of Charge Estimation for Power Battery with Improved Extended Kalman Filter," *IEEE Transactions on Instrumentation and Measurement* 72 (2023): 1-10.
13. Plett, G.L., "Extended Kalman Filtering for Battery Management Systems of LiPB-Based HEV Battery Packs: Part 3. State and Parameter Estimation," *Journal of Power Sources* 134, no. 2 (2004): 277-292.
14. Maletić, F., Deur, J., and Erceg, I., "A Multitimescale Kalman Filter-Based Estimator of Li-Ion Battery Parameters Including Adaptive Coupling of State-of-Charge and Capacity Estimation," *IEEE Transactions on Control Systems Technology* 31, no. 2 (2022): 692-706.
15. Fan, T.-E., Liu, S.-M., Tang, X., and Qu, B., "Simultaneously Estimating Two Battery States by Combining a Long Short-Term Memory Network with an Adaptive Unscented Kalman Filter," *Journal of Energy Storage* 50 (2022): 104553.
16. Chen, L., Wu, X., Lopes, A.M., Yin, L. et al., "Adaptive State-of-Charge Estimation of Lithium-Ion Batteries Based on Square-Root Unscented Kalman Filter," *Energy* 252 (2022): 123972.
17. Priya, R.P. and Sakile, R., "State of Charge Estimation of Lithium-Ion Battery Based on Extended Kalman Filter and Unscented Kalman Filter Techniques," *Energy Storage* 5, no. 3 (2023): e408.
18. Lin, X., Tang, Y., Ren, J., and Wei, Y., "State of Charge Estimation with the Adaptive Unscented Kalman Filter Based on an Accurate Equivalent Circuit Model," *Journal of Energy Storage* 41 (2021): 102840.
19. Xiong, R., Duan, Y., Zhang, K., Lin, D. et al., "State-of Charge Estimation for Onboard $LiFePO_4$ Batteries with Adaptive State Update in Specific Open-Circuit-Voltage Ranges," *Applied Energy* 349 (2023): 121581.
20. Lim, K., Bastawrous, H.A., Duong, V.-H., See, K.W. et al., "Fading Kalman Filter-Based Real-Time State of Charge Estimation in $LiFePO_4$ Battery-Powered Electric Vehicles," *Applied Energy* 169 (2016): 40-48.
21. Sandrabyna, M., Sharma, S., and Basu, S., "A Modified State of Charge Estimation Method for Li-Ion Batteries," *2019 IEEE Transportation Electrification Conference (ITEC-India)*, Bengaluru, India, 2019, 1-5, IEEE.
22. Zhang, K., Xiong, R., Li, Q., Chen, C. et al., "A Novel Pseudo-Open-Circuit Voltage Modeling Method for Accurate State-of Charge Estimation of $LiFePO_4$ Batteries," *Applied Energy* 347 (2023): 121406.
23. Zheng, L., Zhu, J., Wang, G., Lu, D.D.-C. et al., "Differential Voltage Analysis Based State of Charge Estimation Methods for Lithium-Ion Batteries Using Extended Kalman Filter and Particle Filter," *Energy* 158 (2018): 1028-1037.
24. Zheng, L., Zhu, J., Lu, D.D.-C., Wang, G. et al., "Incremental Capacity Analysis and Differential Voltage Analysis Based State of Charge and Capacity Estimation for Lithium-Ion Batteries," *Energy* 150 (2018): 759-769.
25. Koga, S., Camacho-Solorio, L., and Krstic, M., "State Estimation for Lithium-Ion Batteries with Phase Transition Materials via Boundary Observers," *Journal of Dynamic Systems, Measurement, and Control* 143, no. 4 (2021), doi:https://doi.org/10.1115/1.4048779.
26. La Rue, A., Weddle, P.J., Ma, M., Hendricks, C. et al., "State-of-Charge Estimation of $LiFePO_4$–$Li_4Ti_5O_{12}$ Batteries Using History-Dependent Complex-Impedance," *Journal of the Electrochemical Society* 166, no. 16 (2019): A4041.

27. Xu, P., Li, J., Xue, Q., and Sun, F., "A Syncretic State-of-Charge Estimator for $LiFePO_4$ Batteries Leveraging Expansion Force," *Journal of Energy Storage* 50 (2022): 104559.
28. Figueroa-Santos, M.A., Siegel, J.B., and Stefanopoulou, A.G., "Leveraging Cell Expansion Sensing in State of Charge Estimation: Practical Considerations," *Energies* 13, no. 10 (2020): 2653.
29. Allam, A. and Onori, S., "Linearized versus Nonlinear Observability Analysis for Lithium-Ion Battery Dynamics: Why Respecting the Nonlinearities Is Key for Proper Observer Design," *IEEE Access* 9 (2021): 163431-163440, doi:https://doi.org/10.1109/access.2021.3130631.
30. Rubagotti, M., Onori, S., and Rizzoni, G., "Automotive Battery Prognostics Using Dual Extended Kalman Filter," *Proceedings of the ASME 2009 Dynamic Systems and Control Conference. ASME 2009 Dynamic Systems and Control Conference*, Vol. 2, Hollywood, CA, October 12–14, 2009, 257-263, ASME.
31. Bartlett, A., Marcicki, J., Onori, S., Rizzoni, G. et al., "Electrochemical Model-Based State of Charge and Capacity Estimation for a Composite Electrode Lithium-Ion Battery," *IEEE Transactions on Control Systems Technology* 24 (2015): 384-399, doi:https://doi.org/10.1109/tcst.2015.2446947.
32. Zhao, S., Duncan, S.R., and Howey, D.A., "Observability Analysis and State Estimation of Lithium-Ion Batteries in the Presence of Sensor Biases," *IEEE Transactions on Control Systems Technology* 25, no. 1 (2016): 326-333.
33. Fotouhi, A., Auger, D.J., Propp, K., and Longo, S., "Lithium–Sulfur Battery State-of-Charge Observability Analysis and Estimation," *IEEE Transactions on Power Electronics* 33, no. 7 (2017): 5847-5859.
34. Fasolato, S. and Raimondo, D. M., "Observability Analysis of a Li-Ion Cell Equivalent Circuit Model Based on Interval Arithmetic," *2022 IEEE Vehicle Power and Propulsion Conference (VPPC)*, Merced, CA, 2022, 1-7, IEEE.
35. Meng, J., Boukhnifer, M., and Diallo, D., "Lithium-Ion Battery Monitoring and Observability Analysis with Extended Equivalent Circuit Model," *2020 28th Mediterranean Conference on Control and Automation (MED)*, Saint-Raphaël, France, 2020, 764-769, IEEE.
36. Samad, N.A., Kim, Y., Siegel, J.B., and Stefanopoulou, A.G., "Battery Capacity Fading Estimation Using a Force-Based Incremental Capacity Analysis," *Journal of the Electrochemical Society* 163, no. 8 (2016): A1584.
37. Kim, W.-Y., Lee, P.-Y., Kim, J., and Kim, K.-S., "A Nonlinear Open Circuit Voltage Representation Enabling State of Charge Estimation at the Voltage Plateau Region of $LiFePO_4$ Battery," *2020 20th International Conference on Control, Automation and Systems (ICCAS)*, Busan, Korea, 2020, 356-359, IEEE.
38. Shi, X. and Chatzis, M., "An Efficient Algorithm to Test the Observability of Rational Nonlinear Systems with Unmeasured Inputs," *Mechanical Systems and Signal Processing* 165 (2022): 108345.
39. Azkue, M., Miguel, E., Martinez-Laserna, E., Oca, L. et al., "Creating a Robust SoC Estimation Algorithm Based on LSTM Units and Trained with Synthetic Data," *World Electric Vehicle Journal* 14, no. 7 (2023): 197.
40. Lipu, M.H. et al., "Data-Driven State of Charge Estimation of Lithium-Ion Batteries: Algorithms, Implementation Factors, Limitations and Future Trends," *Journal of Cleaner Production* 277 (2020): 124110.
41. Baure, G. and Dubarry, M., "Synthetic vs. Real Driving Cycles: A Comparison of Electric Vehicle Battery Degradation," *Batteries* 5, no. 2 (2019): 42.
42. Mufti, G.M., Rehman, M.U., and Basit, A., "Modelling and Simulation of the Electrical Vehicle Using Matlab and Verifying It by Driving Cycles," *International Journal of Engineering & Technology* 7, no. 4.38 (2018): 871-875.
43. Donateo, T., De Pascalis, C.L., Strafella, L., and Ficarella, A., "Off-Line and On-Line Optimization of the Energy Management Strategy in a Hybrid Electric Helicopter for Urban Air-Mobility," *Aerospace Science and Technology* 113 (2021): 106677, doi:https://doi.org/10.1016/j.ast.2021.106677.
44. https://navystp.com/vtm/print?project=N68335-15-C-0401.
45. Lucero, J.N.E., Sujan, V.A., and Onori, S., "An Experimentally Validated Electro-Thermal EV Battery Pack Model Incorporating Cycle-Life Aging and Cell-to-Cell Variations," *IEEE Transactions on Transportation Electrification* (2024): 1, doi:https://doi.org/10.1109/tte.2024.3365028.
46. Catenaro, E. and Onori, S., "Experimental Data of Lithium-Ion Batteries under Galvanostatic Discharge Tests at Different Rates and Temperatures of Operation," *Data Brief* 35 (2021): 106894, doi:https://doi.org/10.1016/j.dib.2021.106894.
47. Hassan, K.K., "Nonlinear Systems," Department of Electrical and Computer Engineering, Michigan State University, East Lansing, MI, 2002.
48. Plett, G.L., *Battery Management Systems, Volume II: Equivalent-Circuit Methods* (Artech House, 2015)

Appendices

Appendix A: 1C Capacity Test Results

Here, we summarize the 1C capacity test results of the five LFP cells used in this work. The 1C cell capacity test protocol is introduced in Section 2.

TABLE A.1 1C capacity test results for the five LFP cells [Ah].

T	Cell #1	Cell #2	Cell #3	Cell #4	Cell #5
10°C	2.52	2.50	2.49	2.48	2.51
25°C	2.57	2.56	2.56	2.55	2.58
45°C	2.57	2.57	2.54	2.50	2.57

FIGURE B.1 Compare different time constants (RC) with a 7200-s relaxation. (a) Different RC responses against experiment data with a 7200-s relax. (b) Voltage prediction error during the 7200-s relax.

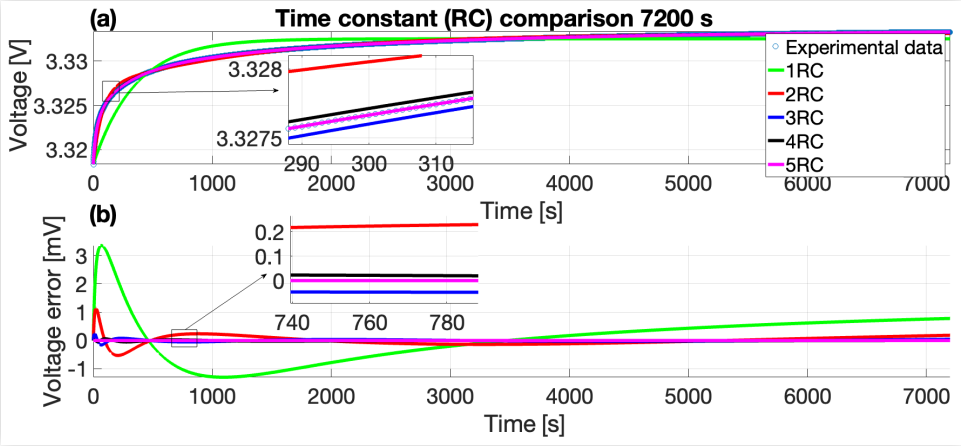

Appendix B: RC Parameter Identification Process and Results

In this section, we detail how the RC parameters of the ECM are identified. The RC parameters are determined based on the experimental GITT data. The GITT test protocol is illustrated in Section 2.

During the relaxation period after each pulse of GITT data, the voltage is determined by the number of time constants, as shown in Figure B.1. As shown in Figure B.1(a), 1 RC pair is insufficient to capture the voltage relaxation, and 2 RC pairs could improve the model prediction significantly compared with 1 RC pair. Increasing the RC pairs will enhance the model prediction capability. To balance the computation time and model accuracy, 2 RC pairs are utilized in this work, resulting in a second-order ECM.

- **For R_0 identification process:** When the current is applied immediately, the voltage drop is considered the consequence of R_0. Therefore, R_0 is calculated as $R_0 = \frac{V_{before} - V_{after}}{I}$, where V_{before} is the voltage before applying the current and V_{after} is the voltage after the current.
- **For time-constants identification process:** When the current becomes 0, the voltage relaxation V_{lax} is controlled by the time constants (τ_1, τ_2) with the following equation.
  $V_{lax} = V_{ini} + \tau_1 \frac{dV_{C1}}{dt} + \tau_2 \frac{dV_{C2}}{dt} - V_{C1,ini} - V_{C2,ini} \cdot V_{ini}$ is the initial relaxation voltage; V_{C1} and V_{C2} are capacitor voltages; $V_{C1,ini}$ and $V_{C2,ini}$ are initial capacitor voltages. The Curve Fitting Toolbox in MATLAB was implemented to fit the time constants based on the voltage relaxation of GITT data as shown in Figure B.1.

FIGURE B.2 (a) RC pair resistance identification process with one discharge pulse and relaxation. (b) Voltage prediction error.

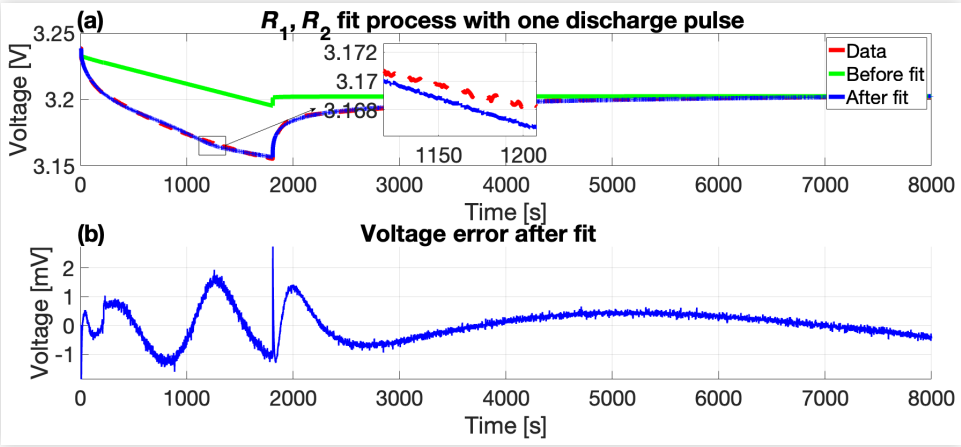

- **For R_1 and R_2 identification process:** Including the discharge pulse and the following relaxation process, the voltage V could be viewed as a function of R_1 and R_2 with the following equation. $V = I * R_0 + \tau_1 \frac{dV_{R1}}{dt} + \tau_2 \frac{dV_{R2}}{dt}$. V_{R1} and V_{R2} are resistance voltages. By fitting this equation to experimental voltage curves, the identified process of R_1 and R_2 at each SOC are shown in Figure B.2. The identified R_0, R_1, R_2, C_1, C_2 are listed in Tables C.2–C.6, respectively.

Appendix C: Q & R values

Here, the process noise covariance matrix Q and sensor noise covariance R for EKF and UKF SOC estimator in this work are summarized.

TABLE C.1 The process noise covariance matrix Q and sensor noise covariance R for EKF and UKF SOC estimator.

	Q	R
EKF	diag(4×10^{4}, 3×10^{-1}, 5×10^{-2})	1×10^{-3}
UKF	diag(2×10^{-19}, 1×10^{-19}, 1×10^{-19})	1×10^{-3}

TABLE C.2 R_0 identification as a function of temperature, C-rate, and SOC [mΩ]. (The parameter values are rounded to integer.)

		SOC										
T	C-rate	0	0.1	0.2	0.3	0.4	0.5	0.6	0.7	0.8	0.9	1
10°C	−2C	16	18	17	17	17	17	18	19	18	16	15
	−1C	17	17	17	17	17	17	17	18	20	17	14
	−0.5C	16	17	16	16	16	16	16	17	17	15	13
	−0.2C	16	18	16	16	16	16	16	16	17	16	14
	0.2C	23	18	17	17	16	16	16	15	15	15	22
	0.5C	22	20	19	18	18	17	17	16	16	15	23
	1C	21	21	21	20	19	19	18	17	17	17	24
	2C	21	21	21	20	20	19	18	18	17	17	24
25°C	−2C	10	10	10	10	10	11	11	12	13	10	7
	−1C	11	12	11	11	12	12	12	12	13	11	10
	−0.5C	11	12	11	11	12	12	12	12	13	14	10
	−0.2C	11	11	11	11	11	11	11	11	12	11	10
	0.2C	16	12	11	11	11	11	11	10	11	10	12
	0.5C	18	14	12	11	11	11	11	11	10	10	14
	1C	19	15	13	12	12	12	12	11	11	11	16
	2C	16	14	13	12	11	11	11	11	10	10	15
45°C	−2C	9	9	9	9	9	9	9	9	9	11	9
	−1C	8	8	8	8	8	8	8	8	8	8	7
	−0.5C	8	8	8	8	8	8	8	8	8	9	7
	−0.2C	9	9	8	8	8	8	8	9	9	8	7
	0.2C	9	8	8	8	8	8	7	7	7	7	8
	0.5C	10	8	8	8	8	8	8	8	8	8	8
	1C	15	9	9	9	9	9	9	9	9	9	10
	2C	11	9	9	9	9	8	8	8	8	8	11

TABLE C.3 R_1 identification as a function of temperature, C-rate, and SOC [mΩ]. (The parameter values are rounded to integer.)

		SOC										
T	**C-rate**	**0**	**0.1**	**0.2**	**0.3**	**0.4**	**0.5**	**0.6**	**0.7**	**0.8**	**0.9**	**1**
10°C	−2C	19	19	12	15	14	16	21	27	27	27	27
	−1C	24	24	15	18	21	24	26	38	56	38	20
	−0.5C	32	32	19	22	27	31	36	43	62	49	37
	−0.2C	66	66	29	30	35	42	45	59	91	89	72
	0.2C	124	85	54	48	43	37	32	48	39	33	300
	0.5C	221	51	44	35	30	25	21	22	27	22	123
	1C	194	75	42	32	26	22	17	16	21	18	62
	2C	155	91	32	24	20	18	14	13	13	14	36
25°C	−2C	13	13	8	10	10	11	14	19	24	18	12
	−1C	18	18	10	12	14	16	18	23	31	24	18
	−0.5C	25	25	12	15	17	20	24	27	47	66	23
	−0.2C	38	38	17	21	26	29	31	42	63	62	61
	0.2C	11	11	23	28	27	23	20	26	27	23	106
	0.5C	47	22	20	23	21	19	16	18	20	16	73
	1C	92	27	21	19	18	15	12	12	17	12	53
	2C	97	35	16	16	15	12	10	9	11	10	28
45°C	−2C	9	9	5	5	7	7	7	9	11	22	7
	−1C	12	12	5	7	8	9	10	11	15	18	18
	−0.5C	18	18	7	9	11	12	13	14	22	30	10
	−0.2C	28	28	7	12	14	17	18	23	31	40	49
	0.2C	10	10	17	14	19	17	15	23	22	17	77
	0.5C	4	4	11	12	13	12	10	13	13	10	33
	1C	5	5	10	9	12	10	8	8	11	7	18
	2C	18	6	8	8	9	8	6	5	8	6	23

TABLE C.4 R_2 identification as a function of temperature, C-rate, and SOC [mΩ]. (The parameter values are rounded to integer.)

		SOC										
T	**C-rate**	**0**	**0.1**	**0.2**	**0.3**	**0.4**	**0.5**	**0.6**	**0.7**	**0.8**	**0.9**	**1**
10°C	−2C	39	39	20	22	34	38	42	25	14	4	4
	−1C	27	60	13	31	27	31	65	17	45	33	22
	−0.5C	63	63	12	34	33	36	48	43	48	67	85
	−0.2C	87	87	16	44	45	50	54	50	86	89	77
	0.2C	201	69	49	77	62	50	31	90	54	37	87
	0.5C	457	63	29	51	47	39	27	54	51	36	87
	1C	503	55	41	49	41	34	31	51	27	32	87
	2C	61	54	49	55	45	30	41	25	39	25	87
25°C	−2C	16	27	12	21	16	28	30	17	17	31	46
	−1C	16	43	8	25	17	23	28	30	17	31	46
	−0.5C	16	49	4	23	30	26	28	20	50	60	52
	−0.2C	16	74	8	37	36	36	40	27	64	58	52
	0.2C	265	47	61	48	43	37	30	46	27	23	65
	0.5C	363	109	37	38	35	31	25	24	32	23	42
	1C	331	78	25	27	29	24	26	22	22	19	42
	2C	285	92	30	31	22	28	19	28	17	21	42
45°C	−2C	32	32	6	16	11	8	17	10	7	25	25
	−1C	36	36	1	15	20	13	14	9	16	18	18
	−0.5C	60	42	1	18	22	16	20	6	23	51	51
	−0.2C	112	60	4	26	37	25	30	9	30	27	24
	0.2C	112	45	21	39	21	20	16	41	13	14	43
	0.5C	172	27	27	21	17	15	12	17	10	11	22
	1C	388	27	34	16	13	13	13	3	14	10	4
	2C	199	33	21	16	14	9	10	11	8	6	4

TABLE C.5 Time constant ($\tau_1 = R_1C_1$) identification as a function of temperature, C-rate, and SOC [s]. (The parameter values are rounded to integer.)

		SOC										
T	**C-rate**	**0**	**0.1**	**0.2**	**0.3**	**0.4**	**0.5**	**0.6**	**0.7**	**0.8**	**0.9**	**1**
10°C	−2C	26	27	36	27	27	36	24	20	17	14	12
	−1C	27	30	40	31	29	34	50	26	27	24	16
	−0.5C	27	31	37	35	32	37	43	50	40	42	38
	−0.2C	23	41	32	34	36	41	47	48	51	50	48
	0.2C	68	73	76	91	85	76	76	108	80	70	68
	0.5C	50	35	37	40	46	37	32	30	50	37	39
	1C	50	30	24	32	38	34	29	27	50	36	33
	2C	15	28	18	25	29	30	26	27	29	37	30
25°C	−2C	21	24	27	23	22	31	46	20	18	15	11
	−1C	24	26	29	30	26	29	36	49	28	25	21
	0.5C	26	28	27	29	30	34	40	46	44	51	33
	0.2C	22	28	23	34	36	39	43	43	50	50	50
	0.2C	22	532	38	39	49	41	41	48	50	45	49
	0.5C	5	45	38	42	48	39	36	48	48	37	38
	1C	18	40	31	39	43	35	30	39	45	30	28
	2C	12	30	23	30	35	31	26	27	45	26	22
45°C	−2C	16	18	19	21	20	22	28	49	20	20	17
	−1C	17	20	19	23	26	29	32	35	29	30	27
	−0.5C	19	22	19	26	32	35	37	36	39	52	43
	−0.2C	16	19	16	24	39	41	37	41	50	50	44
	0.2C	16	889	39	41	48	51	50	52	50	50	50
	0.5C	16	446	36	35	48	42	44	50	43	40	38
	1C	50	28	26	30	50	34	32	37	33	24	23
	2C	38	27	24	28	34	27	22	27	26	17	16

TABLE C.6 Time constant ($\tau_2 = R_2C_2$) identification as a function of temperature, C-rate, and SOC [s]. (The parameter values are rounded to integer.)

		SOC										
T	**C-rate**	**0**	**0.1**	**0.2**	**0.3**	**0.4**	**0.5**	**0.6**	**0.7**	**0.8**	**0.9**	**1**
10°C	−2C	1002	1002	1006	1000	1006	1000	585	962	639	180	337
	−1C	1007	1007	1004	1000	1000	1008	1026	902	835	569	337
	−0.5C	1052	1052	1038	1000	1000	1008	1002	1000	1001	835	364
	−0.2C	1000	1000	1301	1185	1000	1002	1001	1002	1095	834	636
	0.2C	773	2094	1738	1821	1809	1831	1815	2036	1586	1634	1471
	0.5C	802	994	1003	1001	1000	1000	1000	1001	1000	1000	1000
	1C	585	705	792	1000	1000	1000	1001	1000	832	1000	1000
	2C	714	633	587	875	890	1008	1015	1001	677	1007	954
25°C	−2C	866	1020	1020	1011	1039	1002	977	718	1001	358	358
	−1C	1000	1096	1079	1012	1007	1004	993	1025	1001	358	358
	−0.5C	1000	1469	1349	1010	1006	1011	1103	1143	1178	358	358
	−0.2C	1000	1047	1039	1000	1000	1000	1007	1034	990	745	533
	0.2C	1000	2033	1148	1012	1000	1001	1003	1008	1008	1000	1000
	0.5C	1000	3670	1163	1015	1000	1005	1005	1000	1007	1005	1000
	1C	1000	1837	1025	1004	1000	1004	1001	1001	939	999	910
	2C	1000	1649	963	926	1032	1030	1033	1023	763	880	844
45°C	−2C	1000	1010	1007	1002	1001	984	936	903	999	2428	537
	−1C	1000	1010	8070	1012	1033	1011	1094	1040	1093	2394	537
	−0.5C	1000	5873	5520	1002	1007	1007	1220	1204	1135	2394	537
	−0.2C	1000	1017	1005	1008	1000	1000	1000	1011	1017	754	537
	0.2C	1000	1801	1063	1084	1690	1171	1047	1150	1279	1006	993
	0.5C	1000	1801	1063	1042	1002	1001	1003	793	955	943	856
	1C	900	2046	1002	1000	989	1000	977	680	711	793	705
	2C	1000	2465	1044	1014	824	936	842	603	632	707	644